

The formation history and  
palaeoenvironmental significance of  
sedimentary cone deposits in Smoke-  
Tortoise Cave, Naracoorte, South  
Australia.

Thesis submitted in accordance with the requirements of the University of  
Adelaide for an Honours Degree in Environmental Geoscience.

Rhianna Power  
November 2020



THE UNIVERSITY  
*of* ADELAIDE

# **THE FORMATION HISTORY AND PALAEOENVIRONMENTAL SIGNIFICANCE OF SEDIMENTARY CONE DEPOSITS IN SMOKE-TORTOISE CAVE, NARACOORTE, SOUTH AUSTRALIA.**

## **RUNNING TITLE**

Cone Deposit Formation Dynamics

## **ABSTRACT**

Sediment cones represent the main sources of clastic infill for many of the Naracoorte Cave Complex (NCC) cavities. However, the formation history and palaeoenvironmental significance of these cone deposits remain largely unassessed. This study aims to provide improved insights into NCC sediment cone dynamics and tests the hypothesis that the timing of solution pipe openings has a distinctive climatic signature, which could create temporal biases within pitfall fossil deposits. A series of sediment sequences in Smoke-Tortoise Cave (SMT), Naracoorte, including two cone deposits, the sediment floor and a modern analogue deposit, are investigated using geochronological, geochemical, and palaeoenvironmental techniques. By evaluating modern analogue deposits, it is determined that their optically stimulated luminescence (OSL) signal is fully reset prior to entering the cave, providing a modern age of 0 ka and confirming the suitability of OSL dating in this cave setting. Eleven single-grain OSL samples constrain the SMT cone sediments to two distinct depositional events; an older phase at ~305–270 ka (Marine Isotope Stage (MIS) 9 and early MIS 8) and a younger phase at ~230–200 ka (MIS 7), with deposition ceasing for both cones at 200 ka. These results, combined with analyses of published chronological datasets for other NCC cone deposits, imply that there is a climatic control on the opening and closing of solution pipes, with cone deposits preferentially accumulating during warmer interglacial and interstadial climate cycles. The complex histories of solution pipes suggest short-lived, discontinuous opportunities for sediment and fossil accumulation inside the caves, creating potential accumulation biases or gaps in palaeontological records. Comparisons between geochronology and geochemical results reveal that the SMT sediment floor accumulated as the distal part of Cone 2. The absence of pollen in SMT Cave potentially reflects the low preservation potential of pollen from old sediments in closed cave systems.

## **KEYWORDS**

Cone deposits, solution pipes, OSL dating, geochronology, climate, Naracoorte Caves.

## TABLE OF CONTENTS

<b>LIST OF FIGURES AND TABLES .....</b>	<b>3</b>
<b>1.0 INTRODUCTION .....</b>	<b>4</b>
<b>2.0 BACKGROUND.....</b>	<b>8</b>
2.1 Geological Setting .....	8
2.1.1 Naracoorte Deposits .....	9
2.1.2 Study Site – Smoke Tortoise Cave (SMT).....	10
2.2 Solution Pipes and Sedimentary Cone Deposits .....	13
2.3 Single-grain Optically Stimulated Luminescence (OSL) Dating.....	14
2.4 Sediment Geochemistry .....	15
2.5 Pollen Analysis.....	16
<b>3.0 METHODS .....</b>	<b>17</b>
3.1 Sample Collection .....	17
3.1.1 Field Sampling In Smoke-Tortoise Cave .....	17
3.1.2 Laboratory Sample Extraction .....	19
3.2 OSL Dating .....	20
3.2.1 D <sub>e</sub> Determination.....	20
3.2.2 Dose Rate Determination .....	22
3.3 Geochemical Analyses .....	22
3.4 Pollen Analysis.....	23
<b>4.0 RESULTS.....</b>	<b>23</b>
4.1 Core Sequence.....	23
4.2 Pit Excavations.....	23
4.3 Geochronology .....	25
4.4 Geochemistry .....	33
4.5 Pollen.....	37
<b>5.0 DISCUSSION .....</b>	<b>39</b>
5.1 Geochronology .....	39
5.1.1 OSL Dating Interpretations And Suitability.....	39
5.1.2 SMT Sediment Cone Accumulation History .....	40
5.1.3 Inter-Site Comparison Of NCC Sediment Cone Accumulation Trends ....	42

5.2 Geochemistry Interpretations and Regional Comparisons.....	45
5.3 Pollen Preservation Potential .....	46
5.4 Implications for Interpretation of NCC Fossil Records .....	47
5.5 Future Studies.....	48
<b>6.0 CONCLUSION.....</b>	<b>49</b>
<b>ACKNOWLEDGEMENTS.....</b>	<b>50</b>
<b>REFERENCES .....</b>	<b>50</b>
Appendix A: Field Sampling Methods.....	54
Appendix B: Quality Assurance Criteria .....	55
Appendix C: Methods For External Geochemical Analyses .....	57
Appendix D: Pollen Laboratory Process.....	59
Appendix E: XRF Geochemistry Results.....	61
Appendix F: XRD Geochemistry Results .....	65
Appendix G: NCC Cone Deposit Database .....	67
Appendix H: NCC Speleothem Ages.....	69

## LIST OF FIGURES

<b>Figure 1:</b> (a) Diagram of solution pipe opening and sediment cone formation. (b) Cone 1 in Smoke-Tortoise Cave (SMT) .....	7
<b>Figure 2:</b> (a) Topographic map of the Eastern Naracoorte Range (ENR) in relation to the rest of Australia. (b) Location of the NCNP and Smoke-Tortoise Cave.....	9
<b>Figure 3:</b> Map of Smoke-Tortoise Cave with sample locations relevant to this thesis. Redrawn from Cave Exploration Group of South Australia (CEGSA).....	12
<b>Figure 4:</b> OSL dating sample positions. (a) Core 1 & 2. (b) Pit 1 & OSL sample SMT20-A. (c) Pit 2 & OSL sample SMT20-B. (d) Pit 3 & positions of OSL samples SMT20-C, SMT20-D, SMT20-E. ....	18
<b>Figure 5:</b> Procedure for preparation of quartz OSL samples prior to loading into Risø reader. ....	21
<b>Figure 6:</b> (a) Composite photo of opened core (Core 2). (b) Schematic representation of open core.....	24
<b>Figure 7:</b> OSL dose recovery test results for sample SMT20-A. (a) Multiple-grain dose recovery test (b) Radial plot showing the measured/given dose OSL ratios obtained for individual quartz grains in the single-grain SAR dose recovery test .....	26
<b>Figure 8:</b> Radial Plots.....	29
<b>Figure 9:</b> Visual representation of OSL ages for SMT cone, core and sediment floor samples .....	32
<b>Figure 10:</b> (a) LOI (%) content relative to SiO <sub>2</sub> (%) content. (b) Al <sub>2</sub> O <sub>3</sub> (%) content relative to SiO <sub>2</sub> (%) content. (c) Fe <sub>2</sub> O <sub>3</sub> (%) content relative to SiO <sub>2</sub> (%) content .....	34
<b>Figure 11:</b> Variations of XRF major elements (%) and minor elements (ppm) for SMT Core 2 samples.....	36
<b>Figure 12:</b> XRD Pie Charts showing mineralogy .....	38
<b>Figure 13:</b> Comparison of SMT sediment cone ages with marine and ice core palaeoclimate records.....	41
<b>Figure 14:</b> (a) Kernel density estimate (KDE) plot. (b) Distribution of ranked published NCC ages (and 2σ uncertainties) used to construct the KDE plot ( <i>n</i> = 69).....	44

## LIST OF TABLES

<b>Table 1:</b> Summary table of water content, dose rates, De measurements, and final OSL ages for the Smoke-Tortoise Cave samples .....	31
---	----

## 1.0 INTRODUCTION

The Naracoorte cave complex is arguably Australia's richest megafaunal fossil locality and contains extensive palaeoenvironmental sediment archives spanning the last 500 thousand years (ka). There are two main types of cave openings through which sediment can enter this cave system: via roof-collapse or solution pipes. These openings have different effects on cave system dynamics, including the accumulation of sediments and fossil remains (Reed, 2008). Roof-collapse openings typically have wide and open entrances, while solution pipe openings have long, narrow, and vertical structures, and often accumulate distinctive cone-shaped deposits of fallen sediments at their base (White & Webb, 2015) (diagrammatically pictured in Figure 1a). The formation mechanisms and dynamics of these cone deposits are largely unknown; however, elsewhere in Australia it has been postulated that they might be climatically controlled and that their timing of formation coincided with the end of interglacial periods (Lipar et al., 2015, 2017).

The overarching aim of this study is to provide new insights into sedimentary cone characteristics, their ages, and their palaeoclimatic significance in order to better understand the timing and processes leading to their formation; i.e., when they formed, how they formed, and how the timing of their accumulation relates to their surroundings, palaeoecology, and the past climate of the Naracoorte area. To achieve this, the study focuses on optically stimulated luminescence (OSL) dating and geochemical analyses of cone and cave floor deposits at an understudied Naracoorte cave site: Smoke-Tortoise Cave (SMT). One of the main cone deposits of interest (Cone 1) is pictured in Figure 1b. This new data, together with existing data from similar cave

sites associated with solution pipe openings, is used to provide insight into how cone deposits may relate to one another and their environment, and to assess whether there are any inherent fossil accumulation biases associated with megafaunal cave deposits that have accumulated via solution pipe openings.

These goals will be achieved using the following project aims:

- (1) Undertake single-grain OSL dating of a continuous core sequence collected perpendicularly through a well-preserved cone deposit (Cone 1) to determine the duration, timing and rate of sediment accumulation.
- (2) Perform OSL dating on targeted sediment horizons from multiple SMT cone deposits to investigate the range of formation ages at an individual cave site.
- (3) Perform OSL dating on associated sediment floor deposits at SMT to analyse the sediment infill dynamics and geochronology of this particular cave system.
- (4) Examine the suitability of OSL dating for karstic cone deposits, particularly the assumption of prior signal resetting, using a modern age surface sample (SMT20-MA) collected beneath an active solution pipe.
- (5) Analyse the geochemistry (XRF/XRD), composition, stratigraphy, and other sedimentary characteristics (presence of pollen), of the SMT cones and sediment

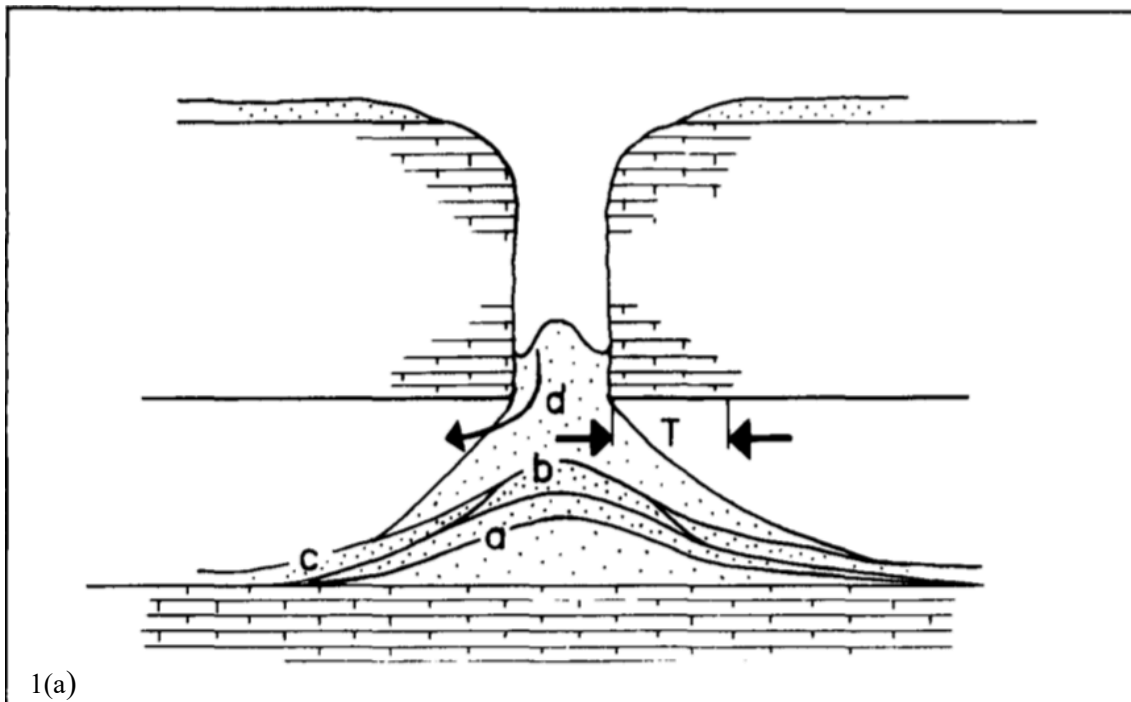
floor in order to better ascertain the external environmental conditions under which they were formed.

- (6) Combine previously published cone deposit ages for the Naracoorte caves with newly obtained ages from this study in order to compare broad-scale temporal relationships between solution pipe formation and significant environmental change (global glacial-interglacial isotopic cycle chronologies).

The main hypothesis for this study states that the cone deposits in Naracoorte caves are formed primarily during interglacial or interstadial periods (warmer and wetter climates) due to enhanced chemical weathering of limestone, which would imply temporal biases in pitfall fossil deposits in these settings. Minor hypotheses include:

- The frequency of cone formation is relatively evenly distributed or follows a regular cycle over the 500 ka time period covered by the Naracoorte cave deposits, implying solution pipe formation is not becoming more or less prevalent over time.
- Cone deposits throughout Naracoorte present a variety of compositions (possibly including pollen), indicative of different surficial environments and palaeoecology at their respective times of formation.
- Individual cone deposits form relatively instantaneously during single and short accumulation events OR cones have complex gradual formation histories involving protracted durations, and multiple (re)activation phases as individual pipes become blocked and unblocked over time.





1(a)



1(b)

**Figure 1: (a) Diagram of solution pipe opening and sediment cone formation, with a, b, and c representing the cone shape for different sediment flow rates. Source: Wells et al. (1984). (b) Photograph of large cone deposit (Cone 1) in the main chamber of Smoke-Tortoise Cave with speleothem growth in the foreground. Photo by Rhianna Power.**

## 2.0 BACKGROUND

### 2.1 Geological Setting

The Naracoorte Caves are located in the far southeast of South Australia and are a part of the Gambier Limestone. The Gambier Limestone formed during the Middle Eocene to the Middle Miocene (Li et al., 2000; White & Webb, 2015), some 12–38 million years ago (Ma), during a time when the land surface was below sea level. This limestone was overlain by layers of sands within the last million years of the Pleistocene (~1 Ma–present day), creating sand dunes which represent remnant coastlines spanning from the Naracoorte Caves Complex (NCC) to the modern coastline of southeast Southern Australia (Cook et al., 1977). These remnant coastlines formed due to a southwest-migrating marine regression over thirteen ice age cycles (Lewis, 2019). Figure 2a shows the eastern-most remnant coastline, also known as the East Naracoorte Range (ENR), which harbours the NCC. The two subsequent remnant coastlines can be seen towards the southwest (shown in olive green/red, and light green colours on Figure 2a), and the ten subsequent coastlines (not pictured) continue parallel with these.

The caves formed between ~0.8–1.1 Ma (White & Webb, 2015). In some areas, groundwater was able to make its way down to the underlying Gambier limestone through fractures caused by movement of the Kanawinka Fault, which led to dissolution of the rock, creating solution pipes and large cave systems (Beck, 2012; Forbes & Bestland, 2007). Extensive caves were created throughout the complex, of which twenty-six are found in the UNESCO World Heritage Naracoorte Caves National Park (NCNP) and attract ~20 thousand visitors annually (Adetutu et al., 2012). In Figure 2b,

the NCNP and Smoke-Tortoise Cave (the focus of this study) are shown to sit along the Kanawinka Fault, which runs parallel to and sits underneath the ENR.

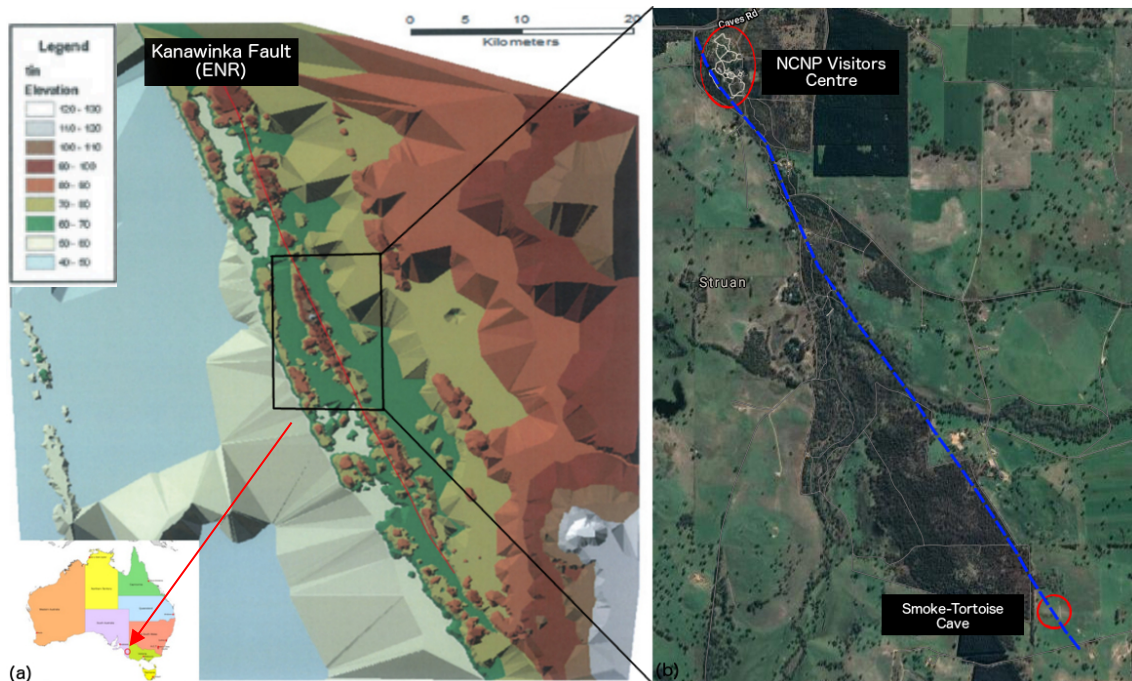


**Figure 2:** (a) Topographic map of the Eastern Naracoorte Range (ENR) and two subsequent remnant coastlines in relation to the rest of Australia. Eocene-Miocene Gambier Limestone (green) is overlain by accumulating sand dunes (red) formed by a regressive southwest-migrating coastline during the Pleistocene. The Naracoorte Caves Complex is located in the centre of the image along the Kanawinka Fault shown in red. Modified from Lewis, I. D. (2019), which is based on Mustafa, S. & Mott, K. (2004, unpublished data). (b) Location of the NCNP (NW) and Smoke-Tortoise Cave (SE), along with the Kanawinka Fault running northwest to southeast (blue dashed line).

### 2.1.1 NARACOORTE DEPOSITS

The Gambier Limestone is made up of predominately grey to cream bryozoan calcarenite with thin layers of marl and clay (Li et al., 2000). The allochthonous sediment deposits that have subsequently infilled the Naracoorte Caves, as described by Forbes & Bestland (2007), are strontium-rich, suggesting that they were originally derived from the Murray-Darling basin and were transported over time by the river to the south-east of Southern Australia. The resulting cave infill is typically a sandy assortment of clastic sediment, fossil material, limestone fragments, and locally derived

organic matter (Forbes & Bestland, 2007). Three types of cave sediments have been defined by Forbes & Bestland (2007): Sediment type I – grey/yellow homogenous sands; sediment type II – brown, organic-rich, sandy silts, and; sediment type III – reddish silts.

A number of chronological and palaeoenvironmental studies have been conducted within the Naracoorte caves (see Section 5.1.3). These studies have primarily focused on speleothems, cave sediment floors, and sediment cone deposits, using a variety of radiometric dating techniques, including accelerator mass spectrometry (AMS) radiocarbon ( $^{14}\text{C}$ ) dating, Uranium-series dating, OSL dating, and electron spin resonance (ESR) dating. Of these study sites, only Victoria Fossil Cave (Grant Hall, Fossil, and Spring/Starburst chambers) and Cathedral Cave (Fossil Chamber) are associated with solution pipe openings; the remainder having roof collapse openings. The published chronological datasets for these four solution pipe cavities provide an important comparative foundation for the results obtained in this thesis. However, it should be noted that the past studies conducted at these sites have not directly examined the temporal or spatial properties of sediment cone dynamics (in particular, their formation mechanics and duration, their relationships with climate, and their sedimentological properties). The present study is therefore the first to explicitly examine broader sediment accumulation trends and relationships for the NCC.

### 2.1.2 STUDY SITE – SMOKE TORTOISE CAVE (SMT)

Smoke-Tortoise Cave (5U20-CEG1182), thought to be discovered around the 1860's from markings on the cave walls, is located immediately southeast of NCNP along the Kanawinka Fault. The main chamber of interest sits approximately 50 m from the main

solution pipe entrance and harbours a large cone deposit (Cone 1), shown in Figure 1b. Numerous speleothems are present throughout the chamber, some creating carbonate caps on top of the cave sediment floor. A second cone deposit (Cone 2) is preserved within SMT beneath a blocked solution pipe opening along a narrow tunnel on the west side of the main chamber. These areas of interest are graphically depicted in Figure 3. SMT has been chosen as the main study site for this thesis as it preserves multiple cone deposits, megafaunal deposits, and no stratigraphical chronology research has been conducted there previously. It therefore provides an ideal location for testing whether different cone deposits in a given cave form synchronously, whether they relate to distinctive climate episodes, and how their stratigraphic relationships can control cave floor infilling and the apparent timing of megafauna records preserved therein.

Very little research has been conducted within the SMT cave system. In 2018, a study focused on U-series dating of speleothems from SMT and associated palaeoclimatic reconstructions. The ages for the sampled SMT speleothems fall into the following time periods: ~10–30 thousand years ago (ka), ~160 ka, ~200 ka, and ~300 ka (Gordon, 2018). These formation ages correspond to periods of enhanced moisture in the soils overlying the caves, either as a result of enhanced precipitation or due to reduced atmospheric temperatures and evaporation losses.

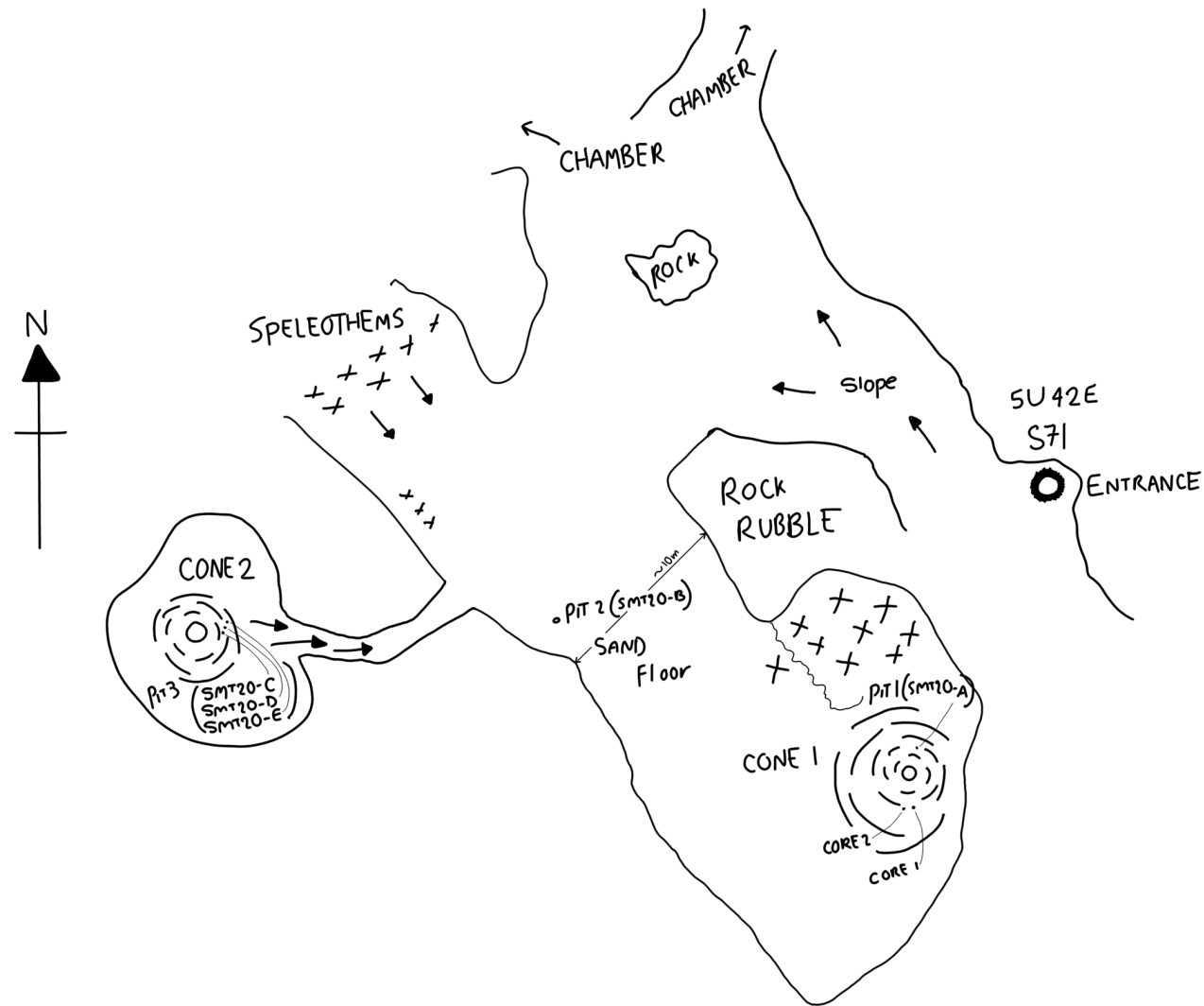


Figure 3: Map of Smoke-Tortoise Cave with sample locations relevant to this thesis. Redrawn from Cave Exploration Group of South Australia (CEGSA).

## 2.2 Solution Pipes and Sedimentary Cone Deposits

Solution pipes are narrow, cylindrical, vertical cavities that form in soluble, carbonate rocks with a porous matrix. They are usually 2–9 m deep but have been found to reach more than 20 m, and their width ranges on average from 0.2–1 m (Jennings, 1968; Lipar et al., 2015). Pipes form by means of chemical weathering and erosion of soluble materials (specifically calcarenite limestone in the Naracoorte area). They are often filled with loose or cemented sediment and allochthonous material derived from overlying palaeosols, or potentially younger surficial sediments/carbonate sands (Lipar et al., 2015).

Their geometry and infill properties support the idea that they form under the influence of gravitational forces (top down), as they sit in the vadose zone directly beneath the palaeosol that directly contributes to their infilling materials. The soils inside these solution pipes add to the speed and intensity of ongoing pipe formation, as they provide carbon dioxide (CO<sub>2</sub>) and organic acids, which increase the aggressiveness of the water passing through the limestone substrate. Other factors that are thought to enhance solution pipe development include surrounding vegetation, animal burrows, surface depressions, structural inhomogeneities, unstable water flow, and climatic influences (Lipar et al., 2015).

Over time, pipes may erode down and open up into a cave system, thus creating an active solution pipe opening. These active openings allow palaeosol material and surface sediments to enter the cave, which typically form a cone deposit at their base (White & Webb, 2015). The repeated blocking and unblocking of these pipes through

time can lead to the accumulation of large cone deposits, potentially representing multi-climatic events.

### **2.3 Single-grain Optically Stimulated Luminescence (OSL) Dating**

Optically stimulated luminescence (OSL) dating provides an estimate of when silicate grains (feldspar and quartz) were last exposed to daylight, and hence can be used to determine the depositional age of clastic sediments (Aitken, 1994; Aitken, 1998; Chithambo, 2018). The technique is based on measuring trapped electron populations that accumulate within lattice defects of mineral grains as a result of exposure to natural radiation and cosmic rays. These charge populations progressively accumulate during the sediment burial period at a rate that is proportional to the level of background radiation, and they can be released (reset) upon exposure to natural or artificial light, resulting in OSL production (Arnold & Demuro, 2018). Measurement of naturally accumulated OSL signals can be used to provide a laboratory estimate of the total radiation dose absorbed by a sediment sample during its burial period (the equivalent dose or  $D_e$ ). To calculate a depositional age for a given sample, the  $D_e$  must be compared with the rate at which the total radiation dose was delivered in the natural burial environment (dose rate), using the following equation (Galbraith & Roberts, 2012):

$$Age (ka) = \frac{D_e (Gy)}{Dose\ rate \left(\frac{Gy}{ka}\right)}$$

OSL dating of quartz grains will be utilised in this project to derive direct depositional ages for the SMT sediment cone and cave floor deposits. OSL quartz dating has been



shown to be reliable for dating sediments spanning the last 400 ka (e.g. Arnold et al., 2016; Arnold & Demuro, 2018), and is therefore suitable, in principle, for dating all currently known infill deposits from the NCC (e.g. Grün et al., 2001; Macken et al., 2011). However, a key assumption of OSL dating is that any residual charge populations accumulated over previous depositional cycles are completely reset by daylight exposure prior to the most recent burial event. If this assumption is not met, then the OSL age is likely to overestimate the true depositional age.

To better characterise the adequacy of signal resetting prior to burial, this study will employ single-grain OSL dating (e.g. Duller, 2008), whereby  $D_e$  values are measured for thousands of individual grains of each sample and the resultant  $D_e$  distributions are used to detect any grain populations that have sizeable residual doses (known as unbleached or partially bleached grains). Additionally, a modern-age, surficial sediment sample will be dated from beneath the active SMT solution pipe opening to test whether it is possible to obtain a modern (fully bleached) OSL age in this cave setting (e.g. Arnold et al., 2019).

## **2.4 Sediment Geochemistry**

The bulk geochemistry of cave infill sediments can provide valuable insights into their elemental and mineralogical makeup, which can then be used to interpret the origin and evolution of accumulated sediments and potentially the climatic conditions they formed under (e.g. degree of surface soil development and weathering) (Forbes & Bestland, 2007). The two most widely used techniques for identifying elements and minerals within Naracoorte cave sediments are X-ray fluorescence (XRF) and X-ray diffraction (XRD) (e.g. Darrénougué et al., 2009; Forbes et al., 2007; Macken et al., 2011). XRF

enables simultaneous identification and quantification of multiple elements within the sample (Jensen et al., 2012). The XRF process involves using high energy X-rays targeted at sub-micron areas of a sample, which causes the sample to emit fluorescent X-rays (or radiation with energy that is characteristic of the elements present) due to excited electrons falling back into their lower orbitals (Jensen et al., 2012). XRD unveils the minerals within a sediment from their crystallographic structure. The process involves the use of monochromatic X-rays beamed onto a sample to create a constructive interference pattern and, in turn, XRD peaks showing what is essentially a fingerprint of the atomic arrangements within the material for mineralogical identification (Forbes & Bestland, 2007; Kohli, 2019). This project uses both quantitative XRD and XRF analyses to determine sediment mineralogies and elemental compositions for the SMT cone and cave floor deposits being targeted for dating.

## **2.5 Pollen Analysis**

Fossil pollen preserved within sediments can provide useful insights into the surrounding surface palaeoenvironments, vegetation, and climate (Barnosky et al., 2004; Bird et al., 2013). Pollen has the potential to accumulate in cave infill deposits as a result of various transportation mechanisms (e.g. dispersal by wind, alluvial and colluvial processes, animals, and scats) but the taphonomic processes can be complex and the likelihood of pollen being preserved in a given cave deposit is highly variable (Hunt & Fiacconi, 2018). Darrénougué et al., (2009) successfully recovered pollen from Blanche Cave sediments that accumulated 36–14 ka through a large roof-window opening. However, the potential for pollen accumulation and preservation in solution pipe cavities and older NCC sediment deposits remains largely unknown. To examine

these inter-site dynamics further, pollen analyses was performed on a subset of sediments collected from SMT cones and sediment floor.

### **3.0 METHODS**

#### **3.1 Sample Collection**

##### **3.1.1 FIELD SAMPLING IN SMOKE-TORTOISE CAVE**

OSL dating, geochemistry and pollen sample collection focused on the two main sedimentary cone deposits preserved in SMT (Cone 1 and 2; SMT20-A, SMT20-C–E) (Figure 4a,b,d), as well as the intervening cave floor deposits that contain megafaunal fossil remains (SMT20-B) (Figure 4c). A “modern-analogue” sample was also taken from beneath the entrance and active solution pipe opening of SMT Cave (SMT20-MA). At Pits 1, 2, and 3, geochemistry and pollen sediment samples were collected from cleaned vertical faces at 5 cm intervals (S1–S22). For detailed field sampling methods, see Appendix A.

In addition to undertaking sample collection, significant features of the cave were noted, along with characteristics of the sediments sampled. Measurements were made of cave dimensions, and floor dip angles through the main chamber.

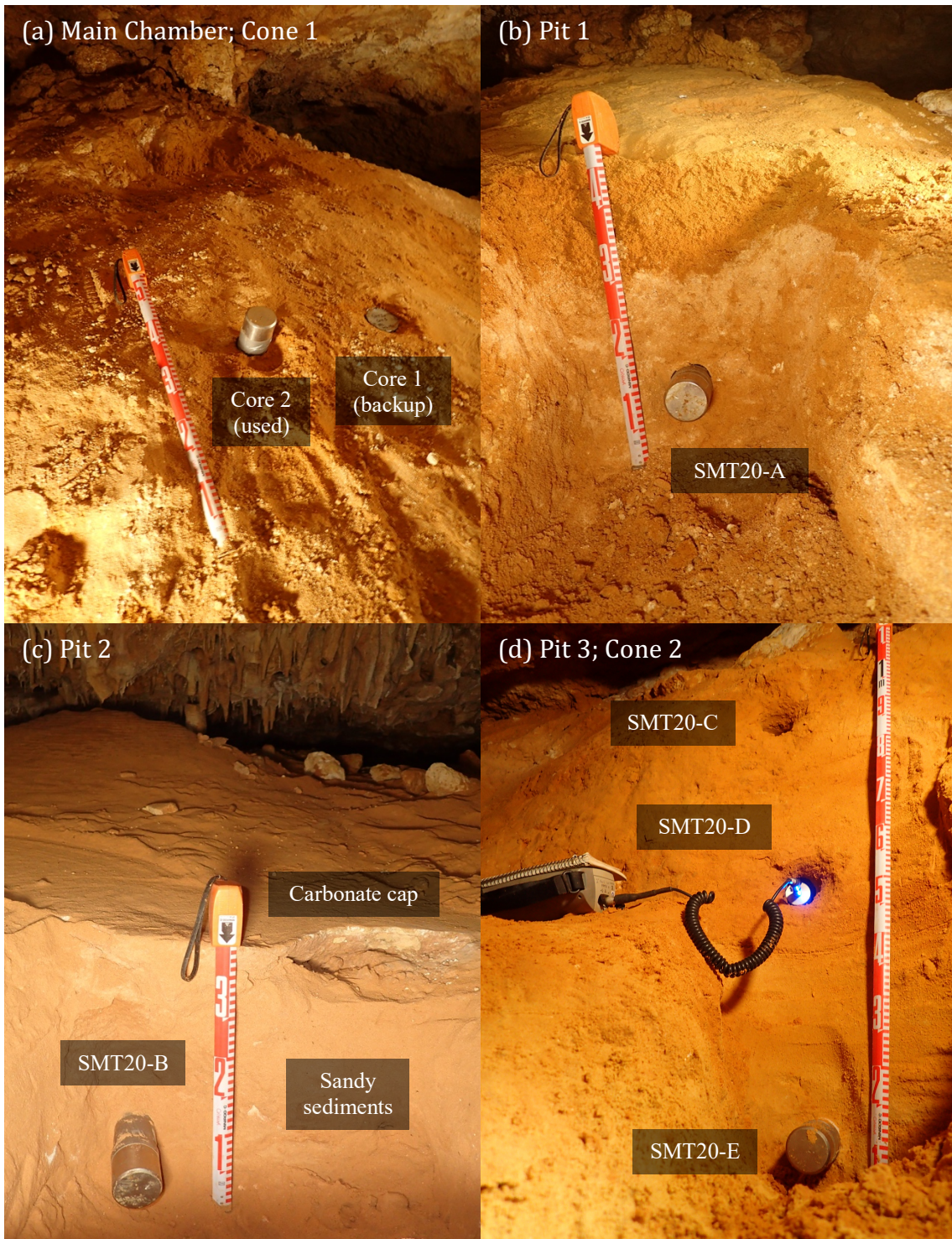


**Figure 4: OSL dating sample positions. (a) Core 1 (backup) & 2 (used in study). (b) Pit 1 showing two distinct layers & OSL sample SMT20-A. (c) Pit 2 with capping carbonate layer above homogenous sands & OSL sample SMT20-B. (d) Pit 3 with field spectrometry measurements underway & the positions of OSL samples SMT20-C, SMT20-D, SMT20-E.**

### 3.1.2 LABORATORY SAMPLE EXTRACTION

Core 2 was sliced in half using a rotary saw and opened under red light conditions that are safe for OSL sampling (605 nm,  $<0.15 \mu\text{W}/\text{cm}^2$ ). Core 1 was set aside as a backup. Five OSL dating samples were extracted at semi-regular intervals along one half of the core to examine the duration of the cone accumulation sequence (SMT20-C19, SMT20-C36, SMT20-C55, SMT20-C65, & SMT20-C94). The OSL samples were taken from depths of 19-24 cm (C19), 36-41 cm (C36), 55-60 cm (C55), 65-70 cm (C65), and 94-99 cm (C94) below the outer cone surface, chosen by visual examination for any changes in sediment appearance. Each OSL sample was collected by first scraping away any disturbed surface material and then extracting the inner, unexposed part of the core (~10 g), taking care to avoid any material in contact with the sides of the PVC tubing. Additional bulk sediment material was taken from the immediate sampling positions (~20 g), and the surrounding 15 cm areas (~20 g) for beta and gamma dose rate measurements, respectively. The opposite half of the core was moved into white light, where it was sub-sampled in 5 cm intervals (SMT20-I1–17) for geochemical analysis.

The six additional OSL samples collected in the field (SMT20-A–E and SMT20-MA) were extracted under dim red-light conditions after discarding any possible light-contaminated material from the ends of the metal tubes. To achieve this, sediment within 2 cm of the ends of each tube was avoided.

## 3.2 OSL Dating

### 3.2.1 $D_e$ DETERMINATION

Purified quartz fractions were prepared for  $D_e$  determination under safe red-light conditions, following the procedures of Aitken (1985). Samples were initially sieved (wet) to 90-250  $\mu\text{m}$  and chemically treated with 30% hydrochloric acid (HCl) to remove carbonates (left for ~45 minutes before rinsing), followed by 30% hydrogen peroxide ( $\text{H}_2\text{O}_2$ ) to remove organics (left overnight). The samples were then rinsed and dried before undergoing heavy liquid density separation to isolate quartz grains (lithium heteropolytungstate (LST) with specific densities of 2.62  $\text{g}/\text{cm}^3$  and 2.72  $\text{g}/\text{cm}^3$ ). The quartz fractions were then re-sieved (dry) to isolate the 212-250  $\mu\text{m}$  fraction used in single-grain OSL studies, etched with 48% hydrofluoric acid (HF) for 40 minutes, and sieved again using a smaller mesh size (180  $\mu\text{m}$ ) to remove any disaggregated grains (Figure 5).

Individual quartz grains were loaded into aluminium discs drilled with a 10 x 10 array of 300  $\mu\text{m}$  holes to ensure true single-grain resolution when making OSL measurements. Single-grain  $D_e$  measurements were made using a Risø TL-DA-20 reader equipped with blue and infrared LEDs, and a 10 mW Nd:YVO<sub>4</sub> single-grain laser attachment emitting at 532 nm. Ultraviolet OSL signals were detected using an Electron Tubes PDM 9107B photomultiplier tube fitted with 7.5 mm-thick Hoya U-340 filters. The single-aliquot regenerative dose (SAR) procedure (Murray & Wintle, 2000) was used to calculate individual  $D_e$  values, which includes a preheat to remove thermally unstable charge contributions and a test dose correction to account for any signal sensitivity changes during repeated OSL measurement cycles. Single-grain OSL  $D_e$

values were obtained by interpolating the sensitivity-corrected natural OSL signal onto a sensitivity-corrected dose response curve that had been obtained by administering a series of known radiation dose to the sample using a calibrated  $^{90}\text{Sr}/^{90}\text{Y}$  beta source.

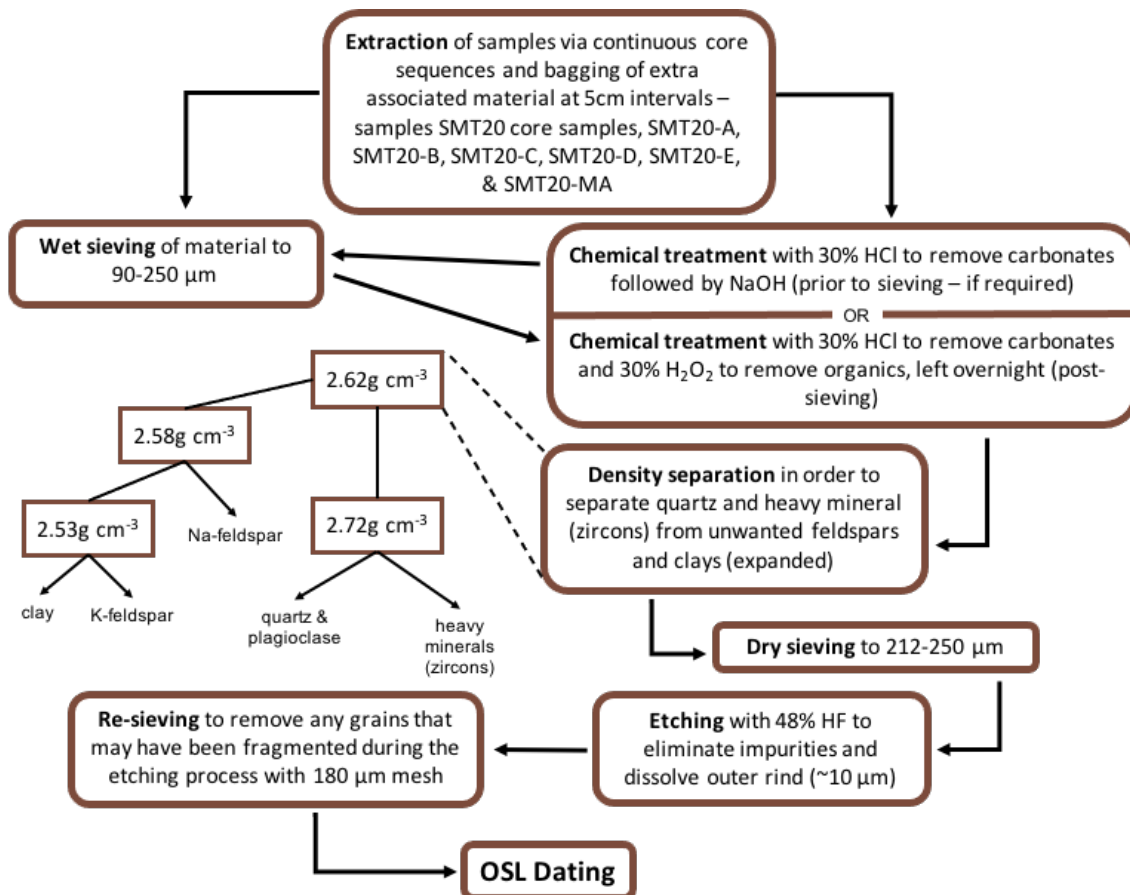


Figure 5: Procedure for preparation of quartz OSL samples prior to loading into Risø reader.

Appropriate SAR preheat conditions were determined with multiple-grain aliquot dose-recovery measurements and confirmed at the single-grain scale using single-grain dose recovery tests. 600 grains were measured per sample, and only those grains that passed a series of quality assurance criteria (as detailed in Appendix B) were included in the final  $D_e$  analysis.

### 3.2.2 DOSE RATE DETERMINATION

The OSL dose rate is derived from the external gamma, beta and cosmic dose rates, with a minor internal dose rate contribution from the quartz grains themselves. Gamma dose rates were determined from *in situ* gamma spectrometry measurements for the OSL samples collected in the field. Each spectrum was collected for 45 minutes, and used to determine sediment U, Th and K concentrations using the energy windows approach described in Arnold et al. (2012). For the Core 2 OSL samples, gamma dose rates were determined using high resolution gamma spectrometry performed on the dried and homogenised bulk sediments collected from the surrounding 15 cm areas, following Fu et al. (2017). External beta dose rates of all samples were determined from measurements made using a Risø GM-25-5 beta counter (Bøtter-Jensen & Mejdahl, 1988) on dried and homogenised bulk sediments collected directly from the OSL sampling positions. Cosmic-ray dose rates were determined using the approach described in Prescott & Hutton (1994), after taking into consideration site altitude, geomagnetic latitude, and density/thickness of sediment and bedrock overburden. The gamma, beta and cosmic dose rates have been corrected for long-term water content (Aitken, 1985) using measurements made on sediment collected from each OSL sample position (weighing before and after drying in a 90 °C oven overnight).

### 3.3 Geochemical Analyses

A total of 50 samples were prepared for external XRF and XRD analyses. Each sample was dried in a 90 °C oven overnight and ground into a fine powder using a Retch MM400 ball mill (oscillating frequency 30 cycles per second for 2 minutes each), before undergoing external analyses at the University of Wollongong, as detailed in Appendix C.



### **3.4 Pollen Analysis**

Pollen analysis was performed on a subset of four sediment samples collected from Pit 1, Pit 2, and Pit 3 to examine the potential for pollen preservation in this setting. Samples were sieved (wet) to <250  $\mu\text{m}$  before being dried and continuing to the laboratory process outlined in Appendix D. Samples were mounted on slides and viewed through a Leica optical microscope at 200x magnification.

## **4.0 RESULTS**

### **4.1 Core Sequence**

Core 2, collected from the main cone deposit (Cone 1), shows a distinct change in stratigraphy at ~65 cm depth, changing from an orange/brown sand to a lighter (yellow/brown to white), coarser carbonate (Figure 6a–b). This carbonate layer begins to gradually transition back to a sandy layer at ~80 cm and returns to being sand dominated at ~95 cm (Figure 6a–b).

### **4.2 Pit Excavations**

Pit 1 is located on the main cone deposit (Cone 1) ~130 cm from the apex of the cone, and on the opposite side from Cores 1 and 2. Two distinct layers are observed. The first extends down to ~15 cm below the top of the exposure and contains orange/brown loose clay sediments, while the second continues to the bottom of the exposure and contains mottled carbonated sediments, unconsolidated white clumps (~1 cm diameter), yellow consolidated clumps (~3 cm diameter), and loose bone fragments that appear to be from a large bone (~1 cm wide) (Figure 4b).

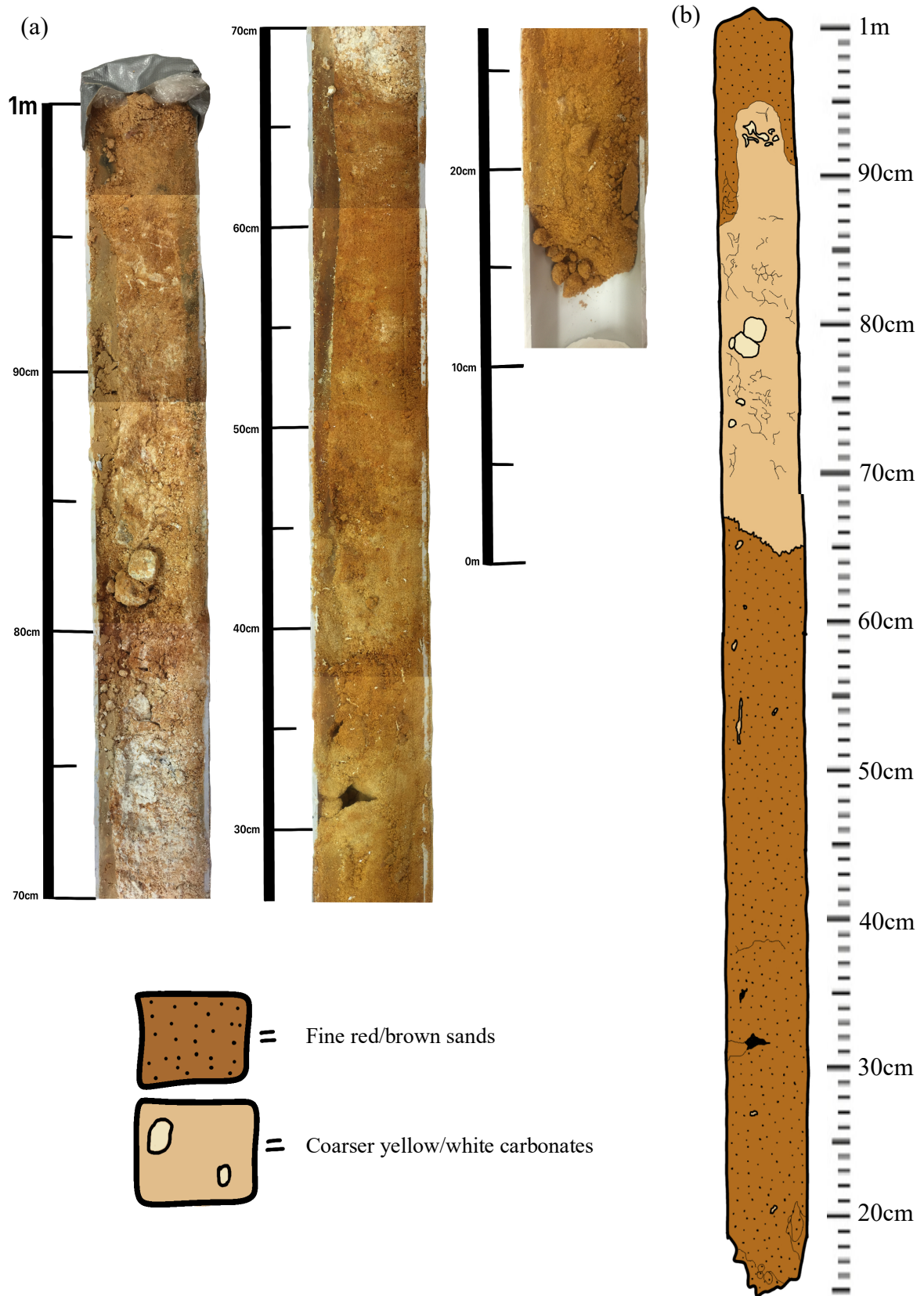


Figure 6: (a) Composite photo of opened core (Core 2). (b) Schematic representation of open core, showing sandy layers compared to carbonate-rich layers.

Pit 2 is located on the cave sediment floor (Figure 3). The exposed face includes a ~10 cm thick speleothem cap-carbonate layer, while the underlying sediments are all homogenous, fine-grained sands, which harbour numerous fossils (megafaunal deposit) (Figure 4c).

Pit 3 is located on the second cone deposit (Cone 2) ~80 cm from the apex of the cone with 28 cm of air space between the sediment surface and the cave ceiling. The upper layer of the exposure spans 66 cm, which consists of large red/brown clay clasts mixed in with finer-grained clay. The lower layer is at least 40 cm thick and displays a transition between the clays and more light, homogenous sands. The sandy layer shows inter-stratification of darker material (potentially clay) between lighter sands (Figure 4d).

### **4.3 Geochronology**

To determine optimal preheat conditions for the SAR procedure, a dose recovery test of various preheat combinations was conducted using multigrain aliquots. A natural/regenerative dose preheat (PH1) of 260°C/10s and a test dose preheat (PH2) of 160°C/10s produced the most suitable measured/given dose ratio ( $0.99 \pm 0.02$ ) (Figure 7a) and test dose correction (mean low and high recycling ratios =  $1.01 \pm 0.01$  and  $1.02 \pm 0.01$ , respectively). The optimum multigrain preheat combination was tested at the single-grain level to confirm its suitability, which showed the weighted mean measured/given dose ratio was consistent with unity at 2 standard errors ( $1.01 \pm 0.01$ ) (Figure 7b). Therefore, these preheat conditions were adopted for single-grain  $D_e$  determination going forward.

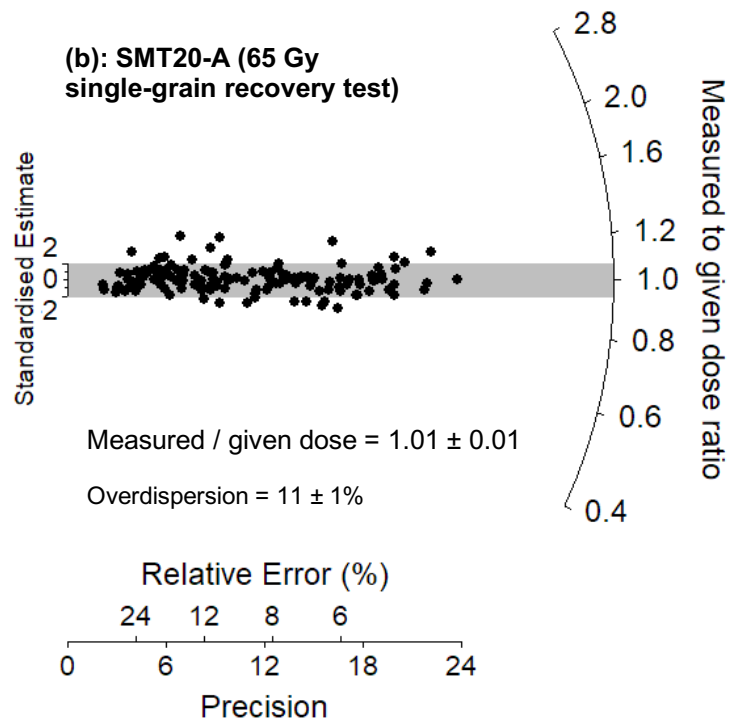
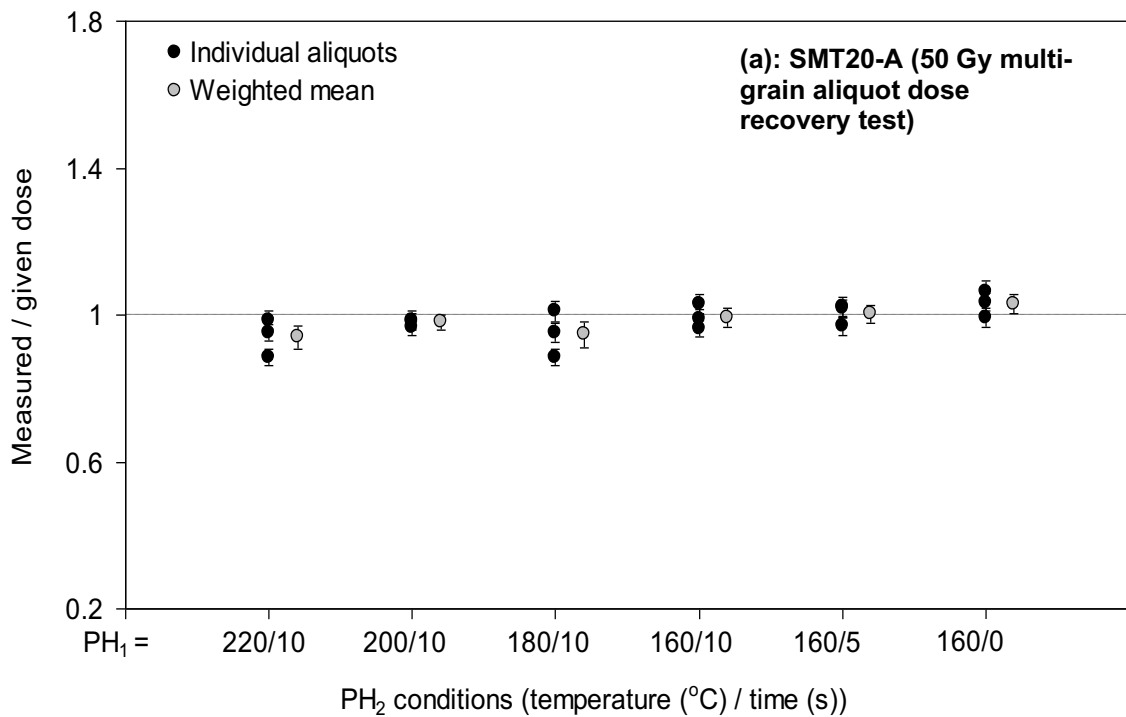


Figure 7: OSL dose recovery test results for sample SMT20-A. (a) Multiple-grain dose recovery test performed using varying test dose preheat temperatures (PH<sub>2</sub>) of 160°C/10s to 220°C/10s. Four aliquots containing ~200 grains were measured for each PH<sub>2</sub> condition (black circles) and used to calculate weighted mean measured/given doses (grey circles). A 50 Gy dose was given to each aliquot in this test, and all measured/given dose ratios are shown with their 2σ uncertainties. (b) Radial plot showing the measured/given dose OSL ratios obtained for individual quartz grains in the single-grain SAR dose recovery test. The grey shaded region is centred on the given dose for each grain (65 Gy).

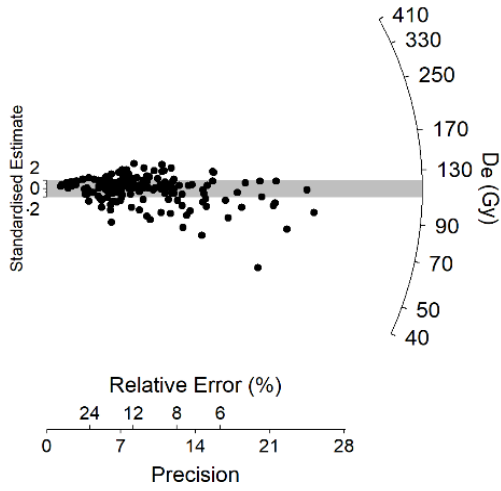
The  $D_e$  distributions for the SMT cone deposits and cave floor cover a wide range of 20–350 Gy (Figure 8). The overdispersion values of individual samples, which indicate the amount of additional scatter in each dataset after taking into consideration the empirical  $D_e$  uncertainties, range from 27–40%, with an average of ~34%. For the NCC samples, overdispersion values of ~20–30% are typically observed for well-bleached samples (e.g., Arnold and Roberts, 2009; Priya, 2018). Six of the SMT cone and cave floor samples have overdispersion values overlapping with the 20–30% range at  $2\sigma$ , though several exhibit slightly higher  $D_e$  dispersion.

Examination of the modern analogue  $D_e$  dataset (SMT20-MA) reveals that the source of overdispersion affecting the SMT dating samples is unlikely to be insufficient bleaching of grains prior to deposition in the cave system (Figure 8). The weighted mean  $D_e$  value of SMT20-MA is  $0.003 \pm 0.002$  Gy, consistent with the expected 0 Gy  $D_e$  value for this modern sample. Moreover, 97.1% of the accepted grains in sample SMT20-MA have an individual  $D_e$  value overlapping with 0 Gy (modern age) at the  $2\sigma$  uncertainty range, confirming that the residual OSL signals have been fully reset by daylight exposure. In accordance with these  $D_e$  distribution characteristics (i.e., fully bleached), the final  $D_e$  values have been obtained using the weighted mean estimates, as determined using the central age model (CAM) of Galbraith et al. (1999) or, in the case of SMT20-MA (which contains negative  $D_e$  values overlapping with 0 Gy at  $2\sigma$ ), the unlogged CAM of Arnold et al. (2009).

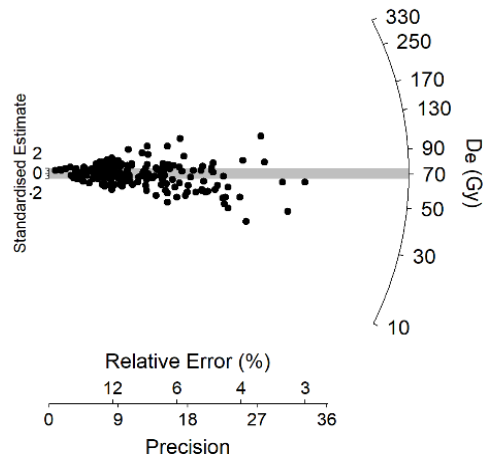
Table 1 summarises the dose rate data and final ages for the SMT OSL samples. The dose rates of these samples are relatively low, ranging from 0.30–0.64 Gy/ka, with the

lowest radioactivities being recorded for the carbonate layer of Core 2 and the homogenous, fine-grained sands of Pit 2. Cone 2 displays decreasing water content with increasing depth (Table 1), while the core sequence from Cone 1 shows the most significant spatial fluctuations in water content, with SMT20-C65 (carbonate-rich sample) containing the largest fraction of water (23.8%).

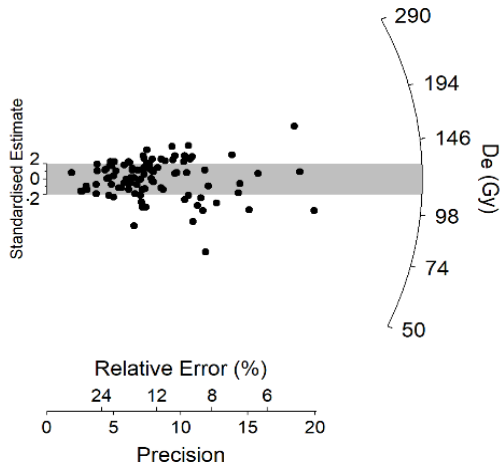
The dated samples primarily span three marine isotope stages (MIS) – MIS 9 (300–337 ka) MIS 8 (243–300 ka) and MIS 7 (191–243 ka) (Lisiecki & Raymo, 2005) (Figure 9). The Core 2 mean ages range from 230 to 305 ka, with a significant jump of ~40 ka between samples SMT20-C55 and SMT20-C65 (Table 1). Samples C19, C36, and C55 correspond to interglacial MIS 7, while C65 is centred on MIS 8 and C94 coincides with interglacial MIS 9. The OSL age of SMT20-A, also from Cone 1, overlaps with the MIS 7 ages of Core 2 samples C19, C36, and C55 at  $2\sigma$ , confirming consistency of the replicate ages from opposing sides of the cone. Cone 2 shows similar results to that of Cone 1 and Pit 1, with mean ages ranging from ~200 to 280 ka, and the most significant gap of ~80 ka occurring between SMT20-C and SMT20-D. SMT20-C correlates with interglacial MIS 7, while both SMT20-D and SMT20-E are centred on early MIS 8 (potentially the MIS 8.5 interstadial at ~275–295 ka; Stirling et al., 2001). The sediment floor yielded a mean age of 270 ka, consistent with the early MIS 8 chronologies obtained for the lower layers of Cone 1 and 2. It appears that deposition of both cone deposits can be separated into two distinct phases: an older phase centred on interglacial MIS 9 or early MIS 8, and a more recent phase centred on the subsequent interglacial (MIS 7). The cones therefore accumulated as multi-depositional events; the youngest of which terminated ~200 ka, with neither of the solution pipes being active since.



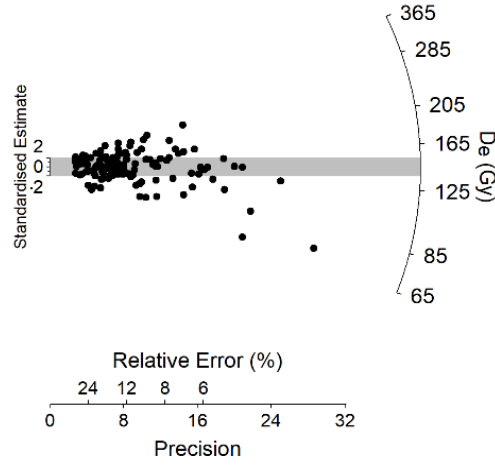
(a): SMT20-A



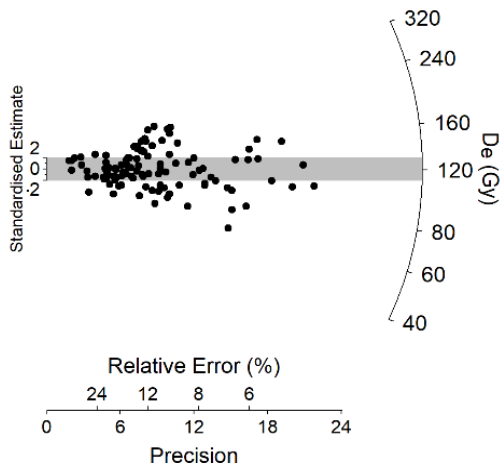
(b): SMT20-B



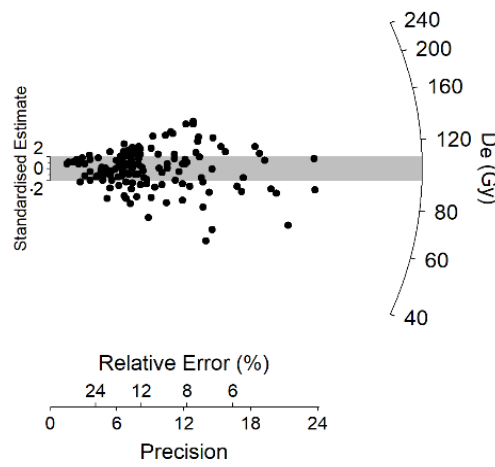
(c): SMT20-C



(d): SMT20-D

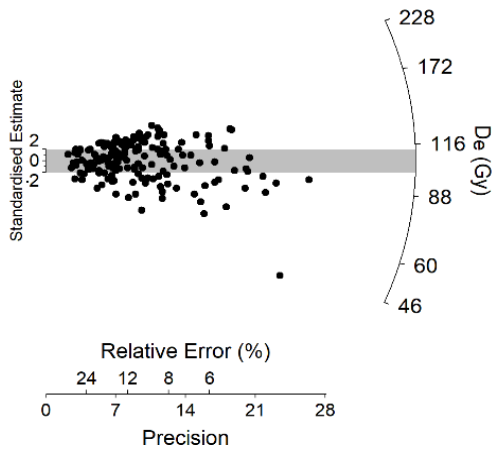


(e): SMT20-E

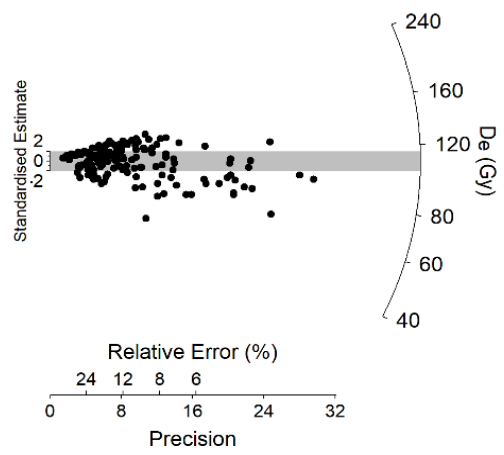


(f): SMT20-C19

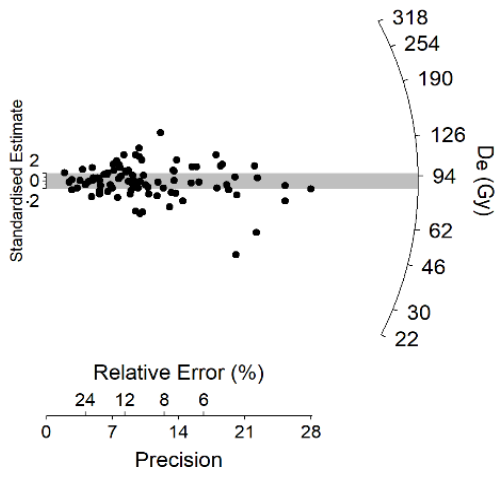
Figure 8: Radial Plots.



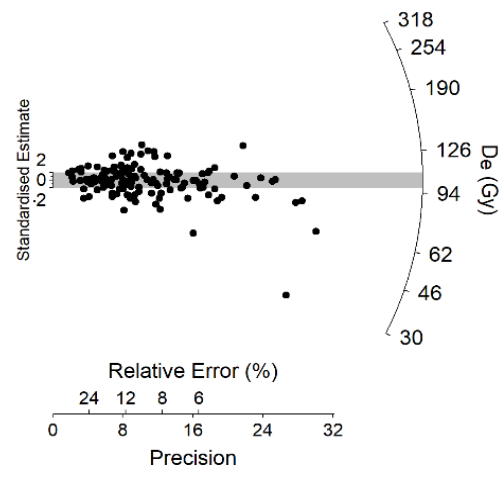
**(g): SMT20-C36**



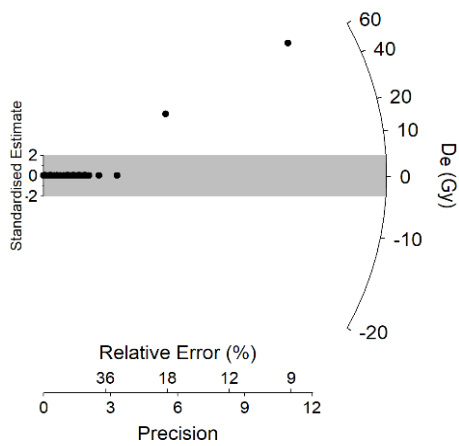
**(h): SMT20-C55**



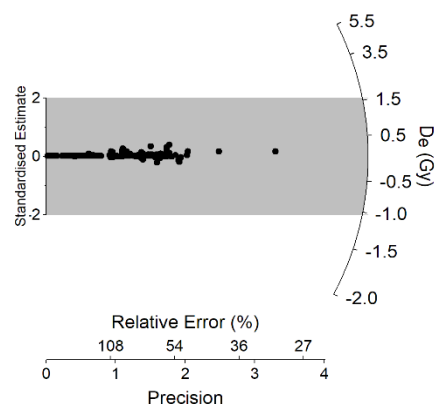
**(i): SMT20-C65**



**(j): SMT20-C94**



**(k): SMT20-MA (all accepted grains)**



**(l): SMT20-MA (minus two high  $D_e$  values)**

**Figure 8 (continued): Radial Plots.**



**Table 1: Summary table of water content, dose rates,  $D_e$  measurements, and final OSL ages for the Smoke-Tortoise Cave samples. Water content values are presented as percentage of dry mass and have been assigned a relative uncertainty of 20% to account for minor variations during burial. The total dose rate includes an internal dose rate of  $0.04 \pm 0.01$  Gy/ka, which has been determined from intrinsic U and Th measurements made on purified (HF etched) quartz grains from a neighbouring site (Bat Cave, NCNP). The final ages are shown with their associated  $1\sigma$  uncertainties.**

Sample	Water Content (%)	Gamma (Gy/ka)	Beta (Gy/ka)	Cosmic (Gy/ka)	Total Dose Rate (Gy/ka)	$D_e$ (Gy)	Final Age (ka)	OD (%)
SMT20-A	13.5	$0.32 \pm 0.02$	$0.18 \pm 0.01$	$0.04 \pm 0.00$	$0.58 \pm 0.03$	$114.93 \pm 3.15$	$198.21 \pm 12.98$	32.6
SMT20-B	1.5	$0.12 \pm 0.01$	$0.11 \pm 0.01$	$0.04 \pm 0.01$	$0.30 \pm 0.02$	$80.85 \pm 2.15$	$270.40 \pm 19.30$	35.7
SMT20-C	10.5	$0.31 \pm 0.02$	$0.22 \pm 0.01$	$0.07 \pm 0.01$	$0.64 \pm 0.03$	$129.35 \pm 3.97$	$202.07 \pm 13.15$	27.0
SMT20-D	8.9	$0.23 \pm 0.01$	$0.22 \pm 0.01$	$0.07 \pm 0.01$	$0.55 \pm 0.03$	$153.57 \pm 4.87$	$278.50 \pm 18.26$	33.0
SMT20-E	3.6	$0.23 \pm 0.01$	$0.14 \pm 0.01$	$0.07 \pm 0.01$	$0.47 \pm 0.03$	$129.69 \pm 4.94$	$278.04 \pm 19.17$	36.6
SMT20-C19	6.1	$0.19 \pm 0.01$	$0.22 \pm 0.01$	$0.04 \pm 0.00$	$0.48 \pm 0.03$	$111.86 \pm 3.53$	$231.00 \pm 15.69$	34.1
SMT20-C36	1.9	$0.20 \pm 0.01$	$0.22 \pm 0.01$	$0.04 \pm 0.00$	$0.50 \pm 0.03$	$116.37 \pm 3.19$	$234.23 \pm 14.75$	33.3
SMT20-C55	6.3	$0.20 \pm 0.01$	$0.25 \pm 0.01$	$0.04 \pm 0.00$	$0.53 \pm 0.03$	$119.34 \pm 3.51$	$227.29 \pm 15.77$	32.8
SMT20-C65	23.8	$0.18 \pm 0.01$	$0.12 \pm 0.01$	$0.04 \pm 0.00$	$0.38 \pm 0.02$	$99.73 \pm 4.36$	$266.14 \pm 21.08$	39.7
SMT20-C94	7.5	$0.15 \pm 0.01$	$0.15 \pm 0.01$	$0.04 \pm 0.00$	$0.37 \pm 0.03$	$113.15 \pm 3.66$	$305.39 \pm 23.42$	36.5
SMT20-MA	7.0	$0.17 \pm 0.01$	$0.31 \pm 0.02$	$0.06 \pm 0.01$	$0.57 \pm 0.03$	$0.003 \pm 0.002$	$0.005 \pm 0.004$	0

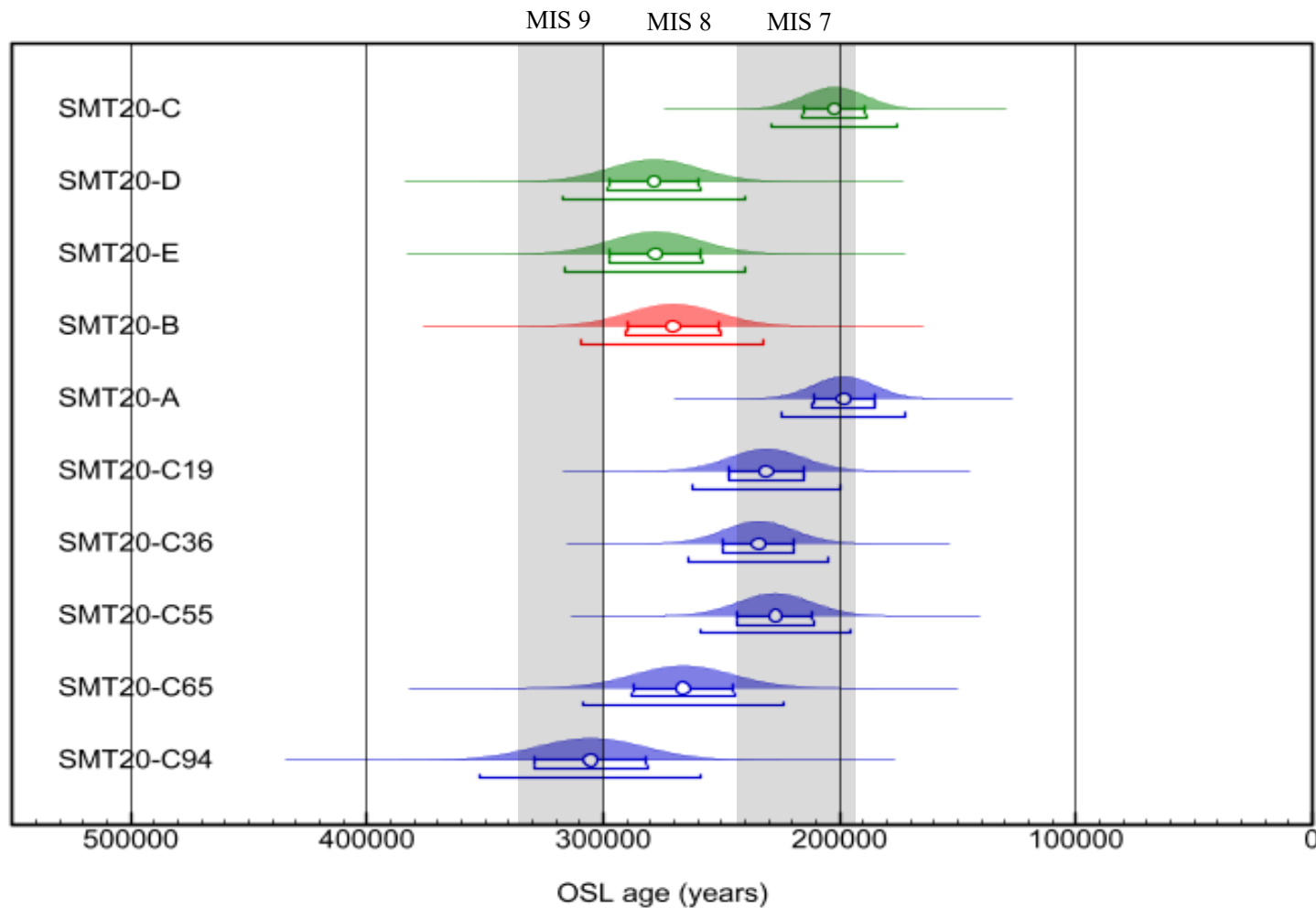


Figure 9: Visual representation of OSL ages for SMT cone, core and sediment floor samples. Blue represents OSL samples from Cone 1 (Pit 1 and Core 2). Red represents OSL samples from the sediment floor (Pit 2). Green represents OSL samples from Cone 2 (Pit 3). A probability density plot is shown for each sample, which is based on  $2\sigma$  uncertainty range of each OSL age estimate. White circles represent the mean ages of the samples, and their associated error bars show the  $1\sigma$  uncertainty ranges. The horizontal bars below this indicate the  $2\sigma$  uncertainty ranges. Marine isotope stage (MIS) boundary ages are taken from Lisiecki & Raymo (2005).

#### 4.4 Geochemistry

The full results of the XRF analysis carried out on the Pit 1, 2 and 3, core 2, and modern age samples are presented in Appendix E, with key trends shown in Figures 10–12. The major element composition of nearly all samples is dominated by  $\text{SiO}_2$ , accounting for ~96% on average in Pit 2 and ~91% in Pit 3, representing homogenous sands, while Pit 1 has a lower  $\text{SiO}_2$  fraction (~68%). Core 2 shows decreasing (from ~95% to ~25%) and then increasing (back up to ~69%)  $\text{SiO}_2$  content with depth, reflecting the presence of an outer sandy layer, followed by a carbonaceous layer at a depth of 65–80 cm, and a second basal sandy layer (see Section 4.1 and Figure 6). Loss on ignition (LOI), which represents all volatiles – organic/inorganic carbon, hydrated materials, and carbonate mineral phase content (Forbes & Bestland, 2007), displays high percentages within Pit 1 (~8–17%) compared to Pits 2 and 3 (average values = 1.3% and 4.7%, respectively), while Core 2 shows a ten-fold increase in LOI from SMT20-I10 downwards (i.e., at a depth of ~65–100 cm, where the sediment changes from being sandy to carbonaceous). LOI also displays a general decreasing trend relative to increasing  $\text{SiO}_2$  content (Figure 10a).  $\text{Al}_2\text{O}_3$  contents range between 0.6% and 17.9% and are again highest in the upper half of Pit 1 (Pit 1 average = ~9.1%), reflecting finer grain sizes and therefore the presence of silts and clays.  $\text{Al}_2\text{O}_3$  content displays an inverse relationship with  $\text{SiO}_2$  content, much like  $\text{Fe}_2\text{O}_3$  (Figure 10b). Similarly,  $\text{Fe}_2\text{O}_3$  contents range from 0.2–7.6% and are highest in the upper layers of Pit 1 (Pit 1 average = ~4%), reflecting the presence of clays and weathering products in this sediment profile (Forbes & Bestland, 2007).  $\text{Fe}_2\text{O}_3$  content shows an inverse relationship with  $\text{SiO}_2$  content in Pits 1 and 3. Pit 2 contains minimal  $\text{Fe}_2\text{O}_3$ , representing predominately sandy sediments (Figure 10c).

Core 2 shows distinctive changes in major and minor element concentrations through the sediment profile (Figure 11). A common change in composition is seen at ~50–55 cm for many elements (Al, Fe, Ca, K, and S). In particular, Ca shows an increase (0.5–27%) below this point, which is mirrored by a sixfold increase of S concentrations. In contrast, Al, Fe, and K all decrease by more than 50% below this depth, before displaying a less marked increase below 70 cm. The uppermost 30 cm of the core is also characterised by >1.8% Al, >1.0% Fe, >0.2 K, and 600 ppm S concentrations.

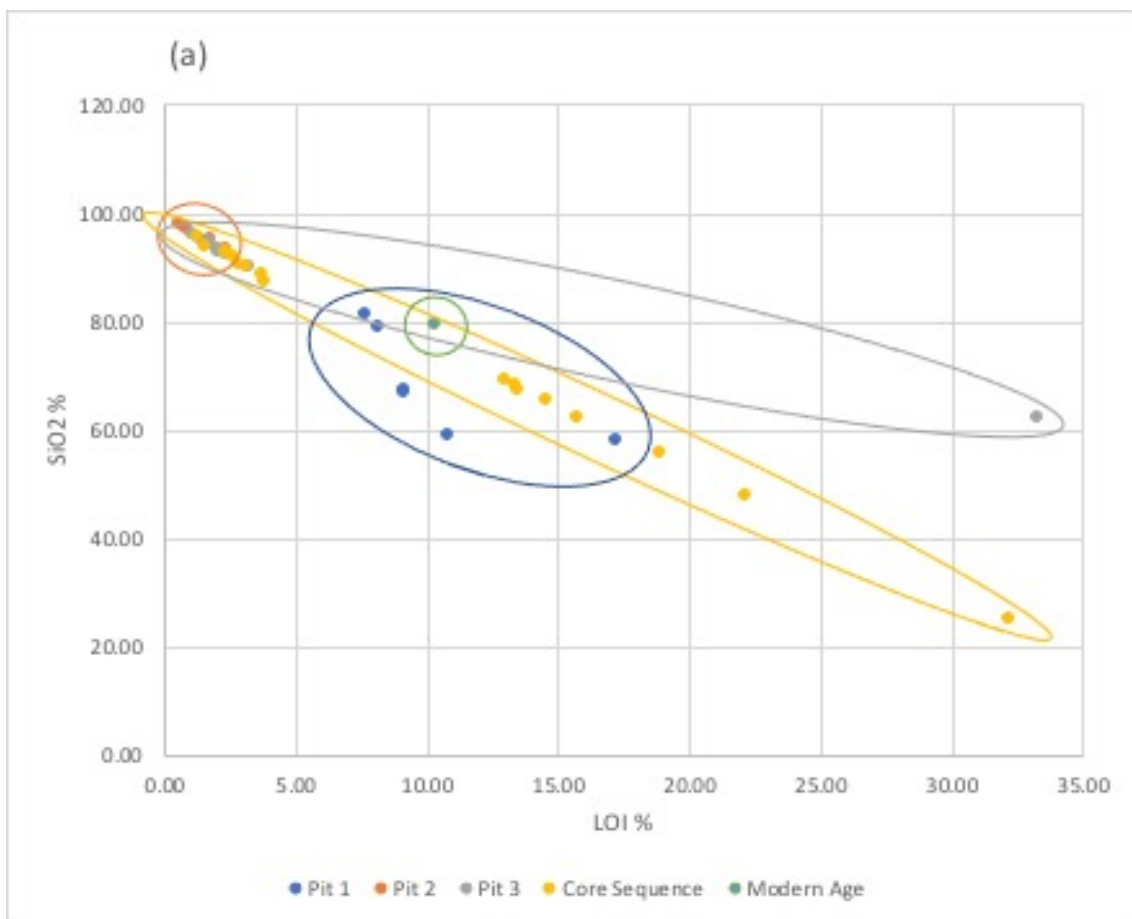


Figure 10: (a) LOI (%) content relative to SiO<sub>2</sub> (%) content.

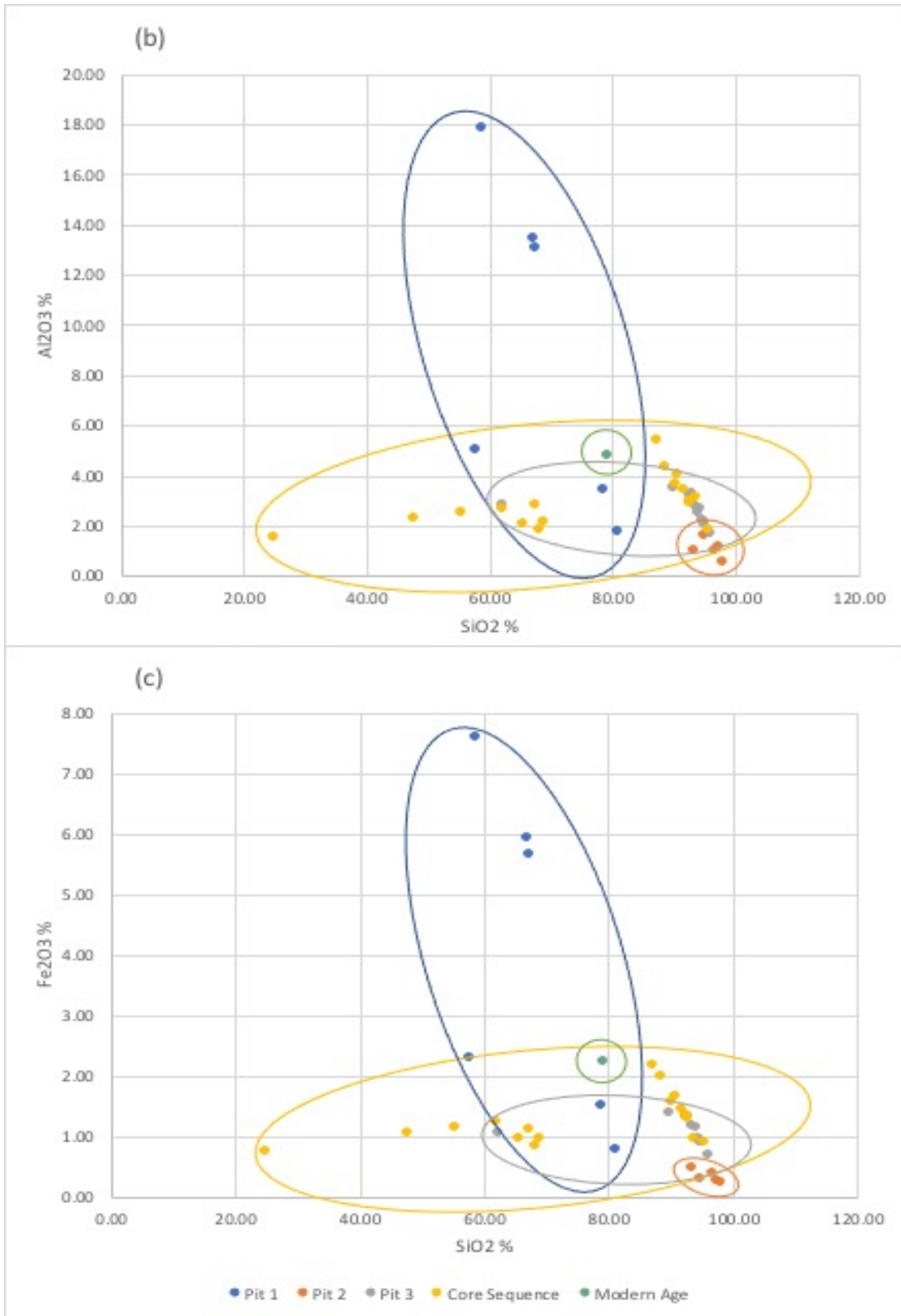


Figure 10 (continued): (b) Al<sub>2</sub>O<sub>3</sub> (%) content relative to SiO<sub>2</sub> (%) content. (c) Fe<sub>2</sub>O<sub>3</sub> (%) content relative to SiO<sub>2</sub> (%) content.

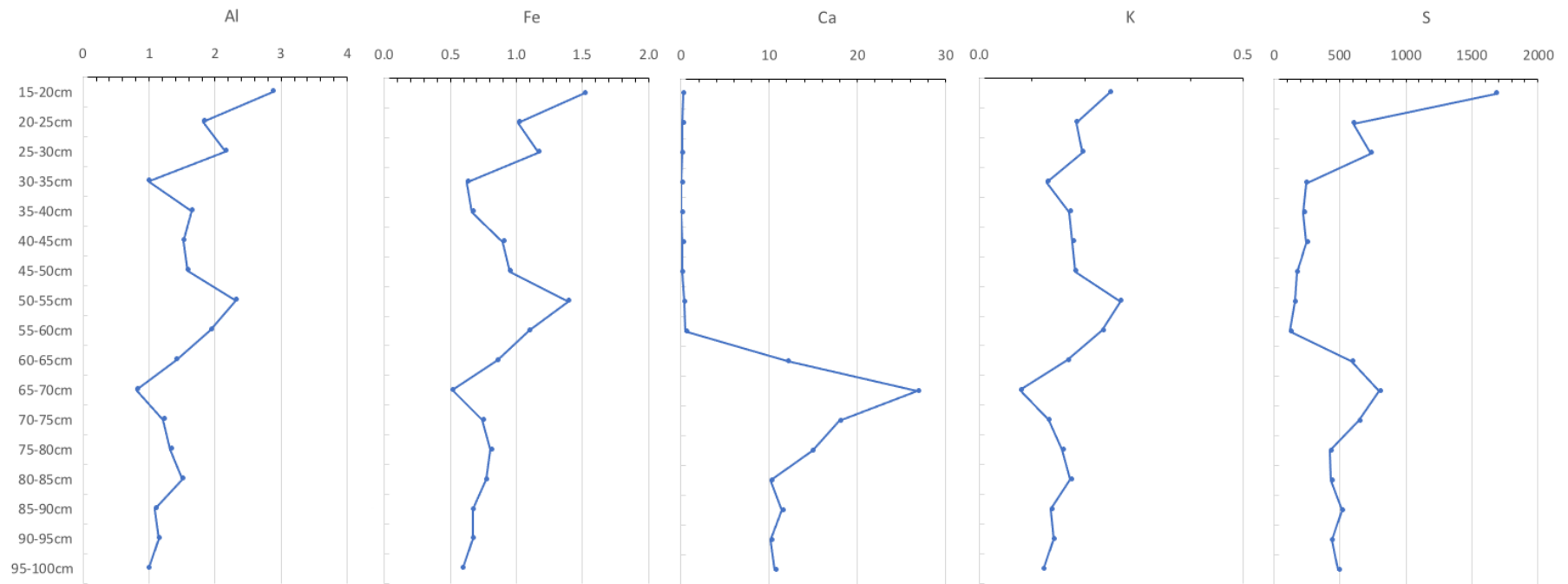


Figure 11: Variations of XRF major elements (%) and minor elements (ppm) for SMT Core 2 samples.

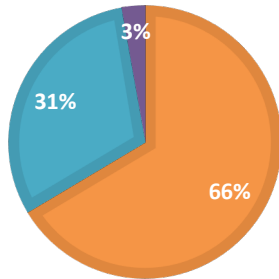
The full results of the XRD analysis for the SMT samples are presented in Appendix F, with key mineralogies shown for representative samples in Figure 12. The sediments from SMT cave are made up of predominately quartz, calcite and chloritoid. Pit 1 is quartz-dominated displaying decreasing chloritoid (27%–0%) and increasing calcite (~4%–>12%) contents with depth. Pit 2 is homogenously quartz-dominated (>97%) with minimal calcite (<3%). Pit 3 is characterised by >90% quartz, with rarely occurring chloritoid and calcite (<7% and <3%, respectively). The mineralogy of Core 2 shows the most significant change with depth, and is characterised by an upper sandy layer and the appearance of calcite at SMT20-I10, followed by decreasing calcite content with depth (~80% at its maximum, to ~30% at the end of the 1 m sequence (Figure 12).

#### **4.5 Pollen**

No pollen was observed in the four initial samples examined in this study; therefore, no additional samples were tested. Few of the introduced lycopodium spikes were present, suggesting procedural problems may have occurred during the preparation of the pollen samples. These complications may have exacerbated the absence of recovered pollen, but the results of this experiment could also describe a genuine absence of any pollen in the SMT sediments.

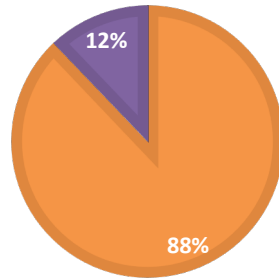
**SMT20 S2 - PIT 1**

■ Quartz  
■ Magnesiochloritoid/Chloritoid  
■ Calcite



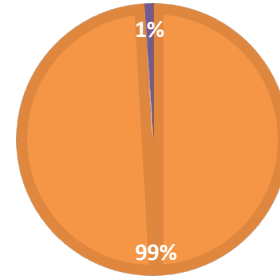
**SMT20 S5 - PIT 1**

■ Quartz  
■ Magnesiochloritoid/Chloritoid  
■ Calcite



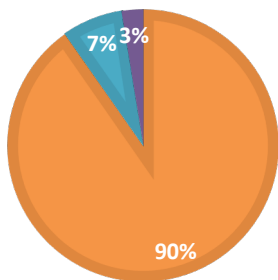
**SMT20 S9 - PIT 2**

■ Quartz  
■ Magnesiochloritoid/Chloritoid  
■ Calcite



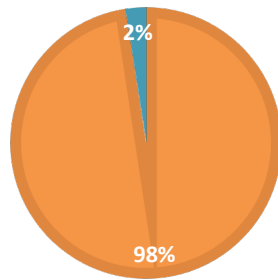
**SMT20 S12 - PIT 3**

■ Quartz  
■ Magnesiochloritoid/Chloritoid  
■ Calcite



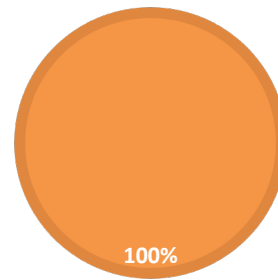
**SMT20 S18 - PIT 3**

■ Quartz  
■ Magnesiochloritoid/Chloritoid  
■ Calcite



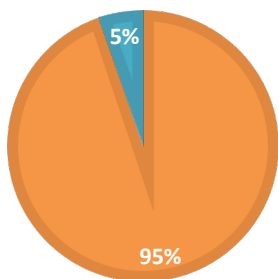
**SMT20 S22 - PIT 3**

■ Quartz  
■ Magnesiochloritoid/Chloritoid  
■ Calcite



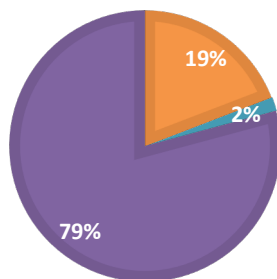
**SMT20 I3 - CORE 2**

■ Quartz  
■ Magnesiochloritoid/Chloritoid  
■ Calcite



**SMT20 I11 - CORE 2**

■ Quartz  
■ Magnesiochloritoid/Chloritoid  
■ Calcite



**SMT20 I15 - CORE 2**

■ Quartz  
■ Magnesiochloritoid/Chloritoid  
■ Calcite

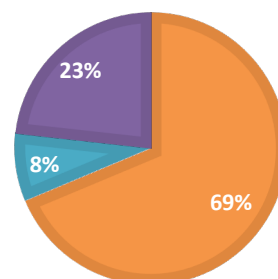


**Figure 12: XRD Pie Charts showing mineralogy.**



## 5.0 DISCUSSION

### 5.1 Geochronology

#### 5.1.1 OSL DATING INTERPRETATIONS AND SUITABILITY

The primary purpose of analysing the modern age analogue sample was to determine whether single-grain OSL is suitable for dating sediments in this solution pipe cave setting. A final age of  $0.005 \pm 0.004$  ka ( $5 \pm 4$  years) was obtained for OSL sample SMT20-MA, which is in agreement with the expected modern age at  $2\sigma$ . Therefore, the assumption that the samples have been fully bleached prior to burial is met and OSL dating can be confirmed a suitable technique. This result is consistent with a recent synthesis study of 19 modern analogue OSL samples from a range of depositional settings (Arnold et al., 2019), which included several surface sediments collected adjacent to solution pipe cave openings.

Given the results of the SMT modern analogue study, the overdispersion observed for the SMT cone and sediment floor samples is primarily attributed to scatter associated with beta-dose heterogeneity (e.g. Nathan et al., 2003) rather than partial bleaching. Variations in beta dose rates received by individual grains are particularly common in relatively homogenous, quartz-rich sands that contain localised radioactivity ‘hotspots’ (e.g. K-feldspars and heavy minerals) and ‘coldspots’ (e.g. carbonate nodules), and can give rise to the types of broadly symmetrical or negatively skewed  $D_e$  distributions seen in this study (e.g. Arnold et al., 2014; Lewis et al., submitted). In such cases, the central age model (CAM) has been showed to yield more reliable estimates of the sample-average burial doses than other age models such as the finite mixture model (e.g.,

Arnold et al., 2014, 2016), underscoring the suitability of the  $D_e$  estimates obtained at SMT cave.

### 5.1.2 SMT SEDIMENT CONE ACCUMULATION HISTORY

The SMT core, cones, and sediment floor samples span MIS 7, 8 and 9 (Figure 13). There are two broad groupings of depositional age for these samples: one in MIS 7, which corresponds to the upper layers of Cone 1 and 2, and a second clustering in MIS 9/early MIS 8, which corresponds to the lower layers of Cone 1 & 2, and the sediment floor. These temporal trends, and their correspondence with distinctive sedimentary units, strongly suggests that each cone accumulated via two separate depositional events, as opposed to continuous accumulation over time.

These sediment accumulation histories in turn provide insights into the opening and closing of the solution pipes associated with Cones 1 and 2. The OSL ages suggest that both solution pipes were open and depositing synchronously at ~300–270 ka, during interglacial MIS 9 and early MIS 8. Stratigraphically, OSL samples SMT20-C55 and SMT20-C65 from Core 2 sit just 5 cm apart; however, their ages reveal a significant gap of ~40 ka, which coincides with a distinctive sedimentological change. This implies that for 40 ka, very little sediment accumulation was occurring. It can then be reasonably assumed that the solution pipes closed (became blocked or choked with sediment and vegetation) at ~270 ka, at which point carbonate deposition began to occur in the near-surface horizons of Core 2. This carbonate deposition episode likely occurred via precipitation of drip waters percolating down through the solution pipe but may have also involved the slow accumulation of fallen limestone clasts and calcite speleothems from the cave ceiling and walls surrounding the cone. Subsequently, both

Cone 1 and 2 show that allochthonous deposition began again during interglacial MIS 7, at ~230 ka for Cone 1 and ~200 ka for Cone 2, suggesting that the solution pipes had reopened at the onset of interglacial MIS 7. The youngest OSL age obtained for both cones is ~200 ka, indicating the final closing of both solution pipes occurred towards the end of interglacial MIS 7.

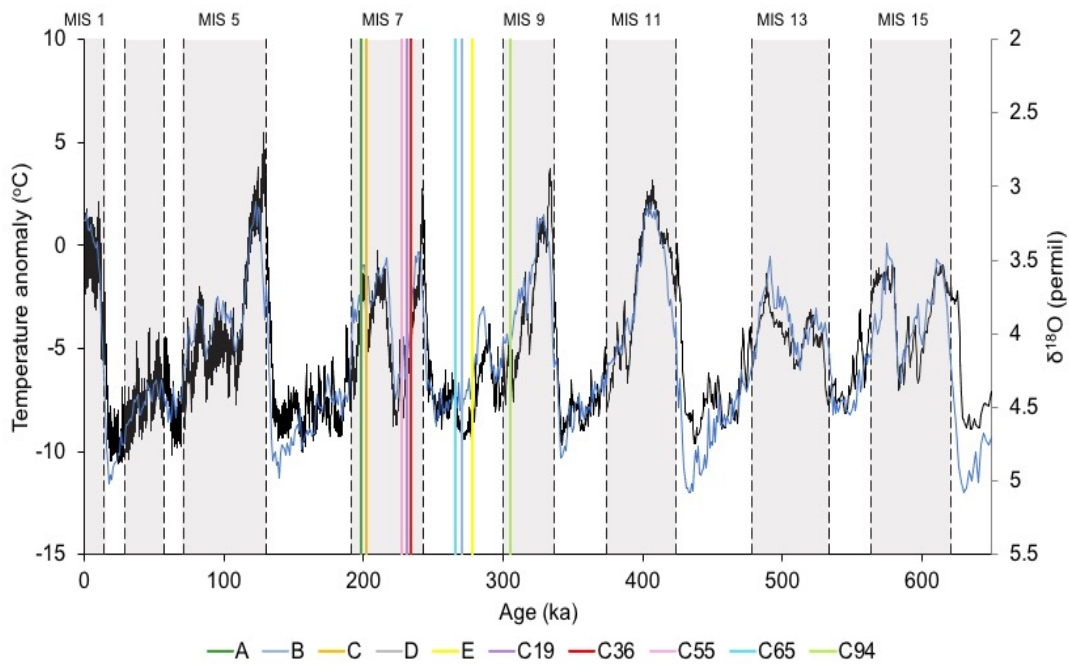


**Figure 13: Comparison of SMT sediment cone ages with marine and ice core palaeoclimate records. The black curve represents the deuterium excess temperature record from EPICA Dome C ice core (Jouzel et al., 2007) (plotted on primary y-axis). The blue curve represents the globally distributed benthic stack  $\delta^{18}\text{O}$  records of Lisiecki & Raymo (2005) (plotted on secondary y-axis). MIS boundary ages taken from Lisiecki & Raymo (2005).**

The sediment floor OSL sample from Pit 2 is chronologically consistent with the lower layers of Cone 2, as well as the deeper layers of Cone 1 (~270 ka) (Figure 9). It seems more likely that the cave floor sediments filling the main SMT chamber were derived primarily from Cone 2, as SMT20-D and SMT20-E were steadily and rapidly depositing during this time (these two samples are separated by ~45 cm stratigraphically, but yield

the same OSL age), while Cone 1 was nearing the end of its deposition. Further support for this interpretation comes from the geochemistry results, as detailed in Section 5.2.

### 5.1.3 INTER-SITE COMPARISON OF NCC SEDIMENT CONE ACCUMULATION TRENDS

A total of 77 numerical ages have been published for sediment cone deposits at other NCC sites (Ayliffe & Veeh, 1988; Ayliffe et al., 1998; Brown & Wells, 2000; Darrénougué et al., 2009; Grealy et al., 2016; Grün et al., 2001; Macken et al., 2011, 2013a, 2013b; Moriarty et al., 2000; Pate et al., 2002, 2006; Prideaux et al., 2007; Roberts et al., 2001; St Pierre et al., 2012). The majority of these ages have been obtained using U-series dating of interbedded calcite ( $n = 38$ ), while the remainder have been obtained by ESR/U-series dating of fossil teeth ( $n = 22$ ) or OSL dating of clastic sediments ( $n = 17$ ). The data gathered from this study, combined with pre-existing data from solution pipe opening caves in the NCC (Appendix G), follows the same general trend of ages, with higher probability densities for samples dating ~205 ka and again at ~290 ka (Figure 14a/b). The 205 ka probability density peak coincides with the latter part of interglacial MIS 7, while the 290 ka peak sits at the beginning of MIS 8, where a prominent interstadial peak is seen (MIS 8e or 8.5: e.g., Stirling et al., 2001) (Figure 13), consistent with ages obtained in this study. These high probabilities support the interpretation that the SMT cones underwent at least two separate depositional events, as well as suggesting that the formation of these cones across the broad NCC region is climatically controlled (forming towards the end of interglacial/interstadial periods, with warmer and wetter conditions). The additional high probability peaks associated with the last interglacial (MIS 5), interglacial MIS 11, and MIS 12 interstadial at ~450 ka, further support the climatic origin of solution pipe formation across the NCC.

The probability density peak at ~205 ka appears twice as high as any other peak within the last 600 ka. There is no evidence to suggest that interglacial MIS 7 was warmer or wetter than MIS 5, 9, or 11, so it is possible that the prevalence for solution pipe opening at this time reflects along the term cause related to progressive limestone erosion over time. Since the emergence of the limestone above the water table 0.8–1.1 Ma, weathering and erosion would have progressively occurred, perhaps leading to significant cumulative structural weaknesses and the crossing of geomorphic thresholds by ~200 ka, causing the large increase in solution pipe openings. Though the number of samples in the NCC dataset is relatively limited ( $n = 77$ ), the probability peak at 205 ka does not appear to originate from preservation bias effects (i.e., the preferential preservation of younger sediment cone records at NCC). Such biases would likely lead to higher probability densities for the youngest climate periods (MIS 1, 3, 5), which is clearly not the case for the NCC dataset.

Speleothem ages within the NCC (Appendix H) exhibit strong overlap with the cone deposit dataset (200–300 ka), suggesting particularly dynamic cave environments during this period. The prominent speleothem growth periods at 200 ka and 300 ka are interpreted as reflecting enhanced soil moisture and warmer conditions during interglacials MIS 7 and 9. The similar timings of speleothem formation and the two SMT solution pipe openings and cone accumulations further suggests the latter were potentially driven by these external environmental conditions.

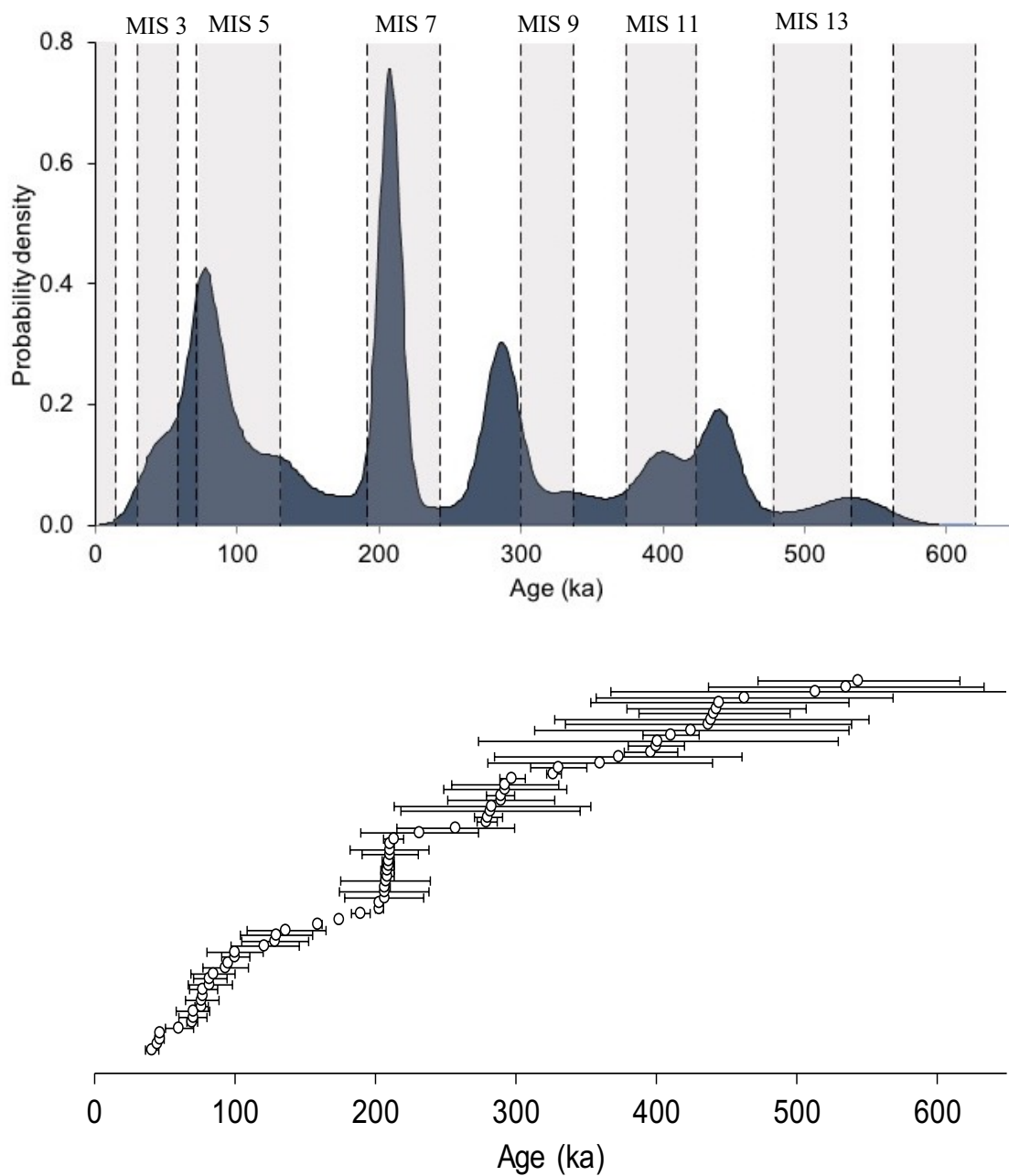


**Figure 14: (a) Kernel density estimate (KDE) plot showing probability densities for all published NCC dating samples from cave sediment sequences associated with solution pipe openings. KDE distribution constructed with DensityPlotter software (Vermeesch, 2012) using an adaptive bandwidth of 6.3 ka (determined using the approach detailed in Silverman (1986) and a shaping parameter of 0.1). (b) Distribution of ranked published NCC ages (and  $2\sigma$  uncertainties) used to construct the KDE plot ( $n = 69$ ).**

There are relatively few well-dated Middle Pleistocene palaeoenvironmental and faunal sequences across the Australian continent spanning 200–300 ka (Fu et al., 2017 (Lake Eyre); Kemp et al., 2020 (Fern Gully Lagoon, QLD); Kershaw et al., 2007; Moss &

Kershaw, 2007 (Lynch's Crater, QLD)), and even fewer well dated MIS 7–9 megafauna deposits (Grün et al., 2001 (Victoria Fossil Cave); Hocknull et al., 2007 (Mt Etna, QLD); Prideaux et al., 2007 (Cathedral Cave)). Therefore, SMT fills an important chronological gap for pursuing future climate and palaeoecological reconstructions in Southern Australia.

## 5.2 Geochemistry Interpretations and Regional Comparisons

The XRF data analysis for SMT shows trends consistent with findings by Forbes & Bestland (2007) for other NCC sites – increasing LOI with decreasing SiO<sub>2</sub> content, and a general increase in Fe<sub>2</sub>O<sub>3</sub>/Al<sub>2</sub>O<sub>3</sub> content with decreasing SiO<sub>2</sub> content (excluding Core 2, which displays consistently low concentrations of Fe<sub>2</sub>O<sub>3</sub>/Al<sub>2</sub>O<sub>3</sub>). High LOI/low SiO<sub>2</sub> represents silt-rich deposits, while low LOI/high SiO<sub>2</sub> represents sandy cave sediments. The Al/Fe/K trends in Core 2 imply that deposition of clays (higher Al/K content) occurred around the same time as increased weathering (higher Fe content) during MIS 7. The large increase in Ca content at ~230 ka signifies deposition of calcite, and the simultaneous variations in S (Figure 11), P and Mg (Appendix E) could imply the presence of gypsum, guano, or degraded limestone during the late MIS 9 interglacial or MIS 8.5 interstadial.

Of the three sediment types defined in Forbes & Bestland (2007), only two are observed within SMT – Sediment types I & III. The sandy deposit horizons of Pit 2 and 3 are similar to sample W2 of Wet Cave analysed by Forbes & Bestland (2007) and correspond to sediment type I with yellow, quartz-dominated sands. Pit 1 seems to display similar geochemistry to samples B2, B8 (Blanche Cave), and WFP1 (Wet Cave) from the same study (Forbes & Bestland, 2007), with the possible appearance of

sediment type III (red silt) in the upper layers (SMT20-S1–4) and sediment type I again in the lower layers (SMT20-S5–6). From the chronologies established at SMT, it could be inferred that sediment types I and III are broadly associated with warmer and wetter conditions. However, both sediment types have been documented for the last glacial maximum (LGM) and stadial deposits associated with MIS 3 at Blanche and Wet Cave. As such, it is likely that these sediment classification types reflect a complex interplay of climate conditions and more localised geomorphic conditions (vegetation cover, transportation, sediment supply).

The XRD results support the interpretation that the origin of the sediment floor (Pit 2) is related to Cone 2 sediments. As Pit 2 and 3 both contain almost identical XRD mineralogies (~98% quartz), and Pit 1 contains no samples matching Pit 2 (<88% quartz), it can be assumed that Cone 2 contributed to the cave floor deposition.

### **5.3 Pollen Preservation Potential**

The absence of pollen in the SMT cave sediments may be genuine or an artifact of the laboratory procedure, as few lycopodium spores were observed in the final slides. If a problem occurred during the sample preparation procedure, it was most likely due to the pouring and rinsing techniques used, or the stringency of the KOH digestion steps. The KOH treatment is used primarily to purify organic rich sediments, and the results of this study may suggest it is worth omitting this phase for the inorganic NCC sediments in future studies. The genuine absence of pollen is also plausible, as the SMT solution pipe openings are small and narrow, which naturally limits the air fall capture potential and prevents much pollen from entering the cave system to begin with. Additionally, the SMT sediments are old compared to other NCC sites that have yielded pollen (e.g.,



Darrénougué et al., 2009), meaning there is more time for pollen to disappear via post depositional oxidation and less chance of preservation. (e.g., Carrión et al., 2009). These findings have implications for the likely success for future pollen studies at similar NCC sites.

#### **5.4 Implications for Interpretation of NCC Fossil Records**

From the data analysed in this study, it can be assumed that NCC sites with solution pipe openings have not remained continuously open and depositing at all times throughout history. Instead they appear to form during distinct periods associated with particular climatic regimes. This means that there are relatively short-lived opportunities for sediment and fossil accumulation alike at individual solution pipe opening caves. Due to this, any fossil records formulated solely from solution pipe opening caves may contain inherent accumulation biases or gaps in palaeontological records for the time periods that coincide with the pipe openings. This bias could have major implications for palaeoecology studies, which have often assumed continuous fossil accumulation over time (e.g., Prideaux et al., 2007). In essence, these palaeoecology studies may represent discontinuous “snapshots” of biodiversity change over successive interglacials or interstadials. To obtain a wider view of palaeontological histories within caves, it may be more beneficial to look at both solution pipe and open-window caves in order to capture the part of the sedimentary record that may not be represented in solution pipe opening caves alone. Such multi-site comparisons will enable more reliable examination of potential sedimentary taphonomic biases and interpretive considerations when reconstructing palaeoecological change from individual cave sites.

## 5.5 Future Studies

This thesis has provided significant new insights into the formation dynamics of solution pipe opening caves and their associated cone deposits, which could be expanded upon to enable much improved interpretations of the NCC cone deposits. In the future, it may prove beneficial to sample deeper into the SMT cones in order to determine whether 300 ka is the maximum age, or if there are older sediments/additional depositional events related to earlier climate cycles. For dating older NCC samples beyond the conventional age range of OSL dating (>400 ka) it would be worth applying novel 'extended-range' luminescence dating techniques such as single-grain thermally transferred OSL dating of quartz, and post-infrared stimulated luminescence dating of K-feldspars (e.g. Arnold et al., 2015, 2019). These approaches have yielded reliable Middle Pleistocene ages at a range of European sites (e.g. Demuro et al., 2020) but have not yet been systematically applied to Australian cave deposits.

Further pollen studies could be performed with a refined preparation method and broader sample set to confirm a lack or presence of pollen preservation in NCC solution pipe caves. If pollen can be found in future studies it will provide valuable information concerning palaeovegetation, which, in turn, could provide additional information about palaeoecology and climate during the time of deposition and solution pipe opening.

Systematic excavations of the SMT sediment floor megafauna deposits should also be undertaken. With the age of the SMT infill now reliably established there is considerable potential to examine the Middle Pleistocene faunal assemblage in the main

chamber and compare palaeoecological trends across several NCC sites spanning MIS 7–9 (Cathedral Cave, Victoria Fossil Cave, SMT).

## **6.0 CONCLUSION**

The sedimentary cone deposits and sediment floor within SMT cave provide invaluable insights into how cone deposits form and under what climate regimes, as well as revealing significant accumulation bias implications for past faunal reconstructions and palaeoecology. SMT Cone 1 preserves two separate depositional events; one from approximately 300–270 ka and the second from ~230–200 ka. Cone 2 also records two separate depositional events; one at approximately 280 ka, and the second concluding around 200 ka. The sediment floor accumulated as the distal part of Cone 2, depositing at ~270 ka, and the geochemistry of the Pit 2 samples are consistent with this shared origin. These distinct depositional events reveal that the opening and closing of solution pipes can be complex. They don't necessarily form continuously over time but are closely controlled by climate, providing a constrained time-window for sediment and fossils to accumulate. This in turn creates the potential for fossil accumulation biases and gaps in the fossil and stratigraphical records, which should be considered when performing palaeontological analysis on closed cave systems. The preservation of pollen can also be affected by the type of cave opening, with the potential for preservation lessening for closed cave systems. Overall, the results of this study support the suitability of single-grain OSL dating at SMT and suggest there is good potential for applying this technique more widely across NCC sites.

## ACKNOWLEDGEMENTS

Firstly, I would like to thank my supervisor, Lee Arnold, and co-supervisors, Liz Reed and Martina Demuro for their ongoing support and feedback throughout the year. Thanks also goes to Katie Howard and Derrick Hasterok. I have greatly appreciated the staff of Prescott Environmental Luminescence Laboratory, including Gillian Ross and Richard Lewis for their guidance and encouragement. I would also like to thank Lloyd White for his involved assistance with external geochemical analyses, as well as Priya for her assistance with the pollen aspects of this thesis. Lastly, I am very grateful for my fellow honours students for giving encouragement when needed this year.

## REFERENCES

- ADETUTU, E., THORPE, K., SHAHSAVARI, E., BOURNE, S., CAO, X., FARD, R., . . . BALL, A. (2012). Bacterial community survey of sediments at Naracoorte Caves, Australia. *International Journal of Speleology*, 41(2), 137-147. doi: 10.5038/1827-806x.41.2.2.
- AITKEN, M. J. (1985). Thermoluminescence dating (Vol. 359): *Academic press London*.
- AITKEN, M. J. (1994). Optical dating: a non-specialist review. *Quaternary Geochronology (Quaternary Science Reviews)*, 13, 503-508.
- AITKEN, M. J. (1998). An Introduction to Optical Dating. *Oxford University Press, Oxford and New York*.
- ARNOLD, L. J., & DEMURO, M. (2018). Dating and optically stimulated luminescence. *The Encyclopedia of Archaeological Sciences*. doi: 10.1002/9781119188230.sasas0151.
- ARNOLD, L. J., DEMURO, M., PARÉS, J. M., ARSUAGA, J. L., ARANBURU, A., BERMÚDEZ DE CASTRO, J. M., & CARBONELL, E. (2014). Luminescence dating and palaeomagnetic age constraint on hominins from Sima de los Huesos, Atapuerca, Spain. *Journal of Human Evolution* 67, 85-107.
- ARNOLD, L. J., DEMURO, M., PARÉS, J. M., PÉREZ-GONZÁLEZ, A., ARSUAGA, J. L., BERMÚDEZ DE CASTRO, J. M., & CARBONELL, E. (2015). Evaluating the suitability of extended-range luminescence dating techniques over early and Middle Pleistocene timescales: Published datasets and case studies from Atapuerca, Spain. *Quaternary International*, 389, 167-190. doi: <https://doi.org/10.1016/j.quaint.2014.08.010>.
- ARNOLD, L. J., DEMURO, M., & RUIZ, M. N. (2012). Empirical insights into multi-grain averaging effects from 'pseudo' single-grain OSL measurements. *Radiation Measurements*, 47(9), 652-658. doi: <https://doi.org/10.1016/j.radmeas.2012.02.005>.
- ARNOLD, L.J., DEMURO, M., SPOONER, N.A., PRIDEAUX, G.J., MCDOWELL, M.C., CAMENS, A.B., ... CARBONELL, E. (2019). Single-grain TT-OSL bleaching characteristics: Insights from modern analogues and OSL dating comparisons. *Quaternary Geochronology*, 49, 45-51.
- ARNOLD, L. J., DUVAL, M., DEMURO, M., SPOONER, N. A., SANTONJA, M., & PÉREZ-GONZÁLEZ, A. (2016). OSL dating of individual quartz 'supergrains' from the Ancient Middle Palaeolithic site of Cuesta de la Bajada, Spain. *Quaternary Geochronology*, 36, 78- 101. doi: <https://doi.org/10.1016/j.quageo.2016.07.003>.
- ARNOLD, L. J., & ROBERTS, R. G. (2009). Stochastic modelling of multi-grain equivalent dose (De) distributions: Implications for OSL dating of sediment mixtures. *Quaternary Geochronology*, 4(3), 204-230. doi: <https://doi.org/10.1016/j.quageo.2008.12.001>.
- ARNOLD, L. J., ROBERTS, R. G. GALBRAITH, R. F., & DELONG, S. B. (2009). A revised burial dose estimation procedure for optical dating of young and modern-age sediments. *Quaternary Geochronology*, 4, 306-325.
- AYLIFFE, L. K., MARIANELLI, P. C., MORIARTY, K. C., WELLS, R. T., MCCULLOCH, M. T., MORTIMER, G. E., & HELLSTROM, J. C. (1998). 500 ka precipitation record from southeastern Australia: Evidence for interglacial relative aridity. *Geology*, 26(2), 147-150.
- AYLIFFE, L. K., & VEEH, H. H. (1988). Uranium-series dating of speleothems and bones from Victoria Cave, Naracoorte, South Australia. *Chemical Geology (Isotope Geoscience Section)*, 72, 211-234.
- BARNOSKY, A. D., KOCH, P. L., FERANEC, R. S., WING, S. L., & SHABEL, A. B. (2004). Assessing the causes of Late Pleistocene extinctions on the continents. *Science*, 306, 70-74.
- BECK, B. (2012). Soil piping and sinkhole failures. *Encyclopedia of Caves*, 718-723.

- BIRD, M. I., HUTLEY, L. B., LAWES, M. J., LLOYD, J., LULY, J. G., RIDD, P. V., ... WURSTER, C. M. (2013). Humans, megafauna and environmental change in tropical Australia. *Journal of Quaternary Science*, 28(5), 439-452. doi: 10.1002/jqs.2639.
- BØTTER-JENSEN, L., & MEJDAHL, V. (1988). Assessment of beta dose-rate using a GM multicounter system. *International Journal of Radiation Applications and Instrumentation*, 14(1-2), 187-191. doi: [https://doi.org/10.1016/1359-0189\(88\)90062-3](https://doi.org/10.1016/1359-0189(88)90062-3).
- BROWN, S. P., WELLS, R. T. (2000). A middle Pleistocene vertebrate fossil assemblage from Cathedral Cave, Naracoorte, South Australia. *Transactions of the Royal Society of S. Australia*, 124(2), 91-104).
- CARRIÓN, J., FERNÁNDEZ, S., GONZALEZ SAMPERIZ, P., LEROY, S. A. G., BAILEY, G., LÓPEZ-SÁEZ, J. A., ... DUPRÉ, M. (2009). *Quaternary pollen analysis in the Iberian Peninsula: the value of negative results* (Vol. 25).
- CHITHAMBO, M. L. (2018). An introduction to time-resolved optically stimulated luminescence. *Morgan & Claypool Publishers*.
- COOK, P. J., COLWELL, J. B., FIRMAN, J. B., LINDSAY, J. M., SCHWEBEL, D. A., & VON DER BORCH, C. C. (1977). The late Cainozoic sequence of southeast South Australia and Pleistocene sea-level changes. *BMR Journal of Australian Geology and Geophysics*, 2, 81-88.
- DARRÉNOUGUÉ, N., DE DECKKER, P., FITZSIMMONS, K. E., NORMAN, M. D., REED, L., VAN DER KAARS, S., & FALLON, S. (2009). A late Pleistocene record of aeolian sedimentation in Blanche Cave, Naracoorte, South Australia. *Quaternary Science Reviews*, 28(25), 2600-2615. doi: <https://doi.org/10.1016/j.quascirev.2009.05.021>.
- DEMURO, M., ARNOLD, L. J., DUVAL, M., MÉNDEZ-QUINTAS, E., SANTONJA, M., & PÉREZ-GONZÁLEZ, A. (2020). Refining the chronology of Acheulean deposits at Porto Maior in the river Miño basin (Galicia, Spain) using a comparative luminescence and ESR dating approach. *Quaternary International*, 556, 96-112.
- DULLER, G. A. T. (2008). Luminescence Dating: Guidelines on using luminescence dating in archaeology. *Swindon: English Heritage*. 43.
- FORBES, M. S., BESTLAND, E. A., WELLS, R. T., & KRULL, E. S. (2007). Palaeoenvironmental reconstruction of the Late Pleistocene to Early Holocene Robertson Cave sedimentary deposit, Naracoorte, South Australia. *Australian Journal of Earth Sciences*, 54(4), 541-559. doi: 10.1080/08120090601078388.
- FORBES, M. S., & BESTLAND, E. A. (2007). Origin of the sedimentary deposits of the Naracoorte Caves, South Australia. *Geomorphology*, 86(3-4), 369-392.
- FU, X., COHEN, T. J., & ARNOLD, L. J. (2017). Extending the record of lacustrine phases beyond the last interglacial for Lake Eyre in Central Australia using luminescence dating. *Quaternary Science Reviews*, 162, 88-110. doi: <https://doi.org/10.1016/j.quascirev.2017.03.002>.
- GALBRAITH, R. F., ROBERTS, R. G., LASLETT, G. M., YOSHIDA, H. & OLLEY, J. M. (1999). Optical dating of single grains of quartz from Jinmium rock shelter, northern Australia. Part I: experimental design and statistical models. *Archaeometry* 41, 339-364.
- GALBRAITH, R. F., & ROBERTS, R. G. (2012). Statistical aspects of equivalent dose and error calculation and display in OSL dating: An overview and some recommendations. *Quaternary Geochronology*, 11, 1-27. doi: <https://doi.org/10.1016/j.quageo.2012.04.020>.
- GORDON, J. (2018). *Speleothem-based explorations of millennial-scale climate change in southern Australasia*. (Master's thesis, The University of Melbourne, Australia). Retrieved from <https://minerva-access.unimelb.edu.au/handle/11343/219704>.
- GREALY, A., MACKEN, A., ALLENTOFT, M. E., RAWLENCE, N. J., REED, E., & BUNCE, M. (2016). An assessment of ancient DNA preservation in Holocene–Pleistocene fossil bone excavated from the world heritage Naracoorte Caves, South Australia. *Journal of Quaternary Science*, 9999(9999), 1-13.
- GRUN, R., MORIARTY, K., & WELLS, R. (2001). Electron spin resonance dating of the fossil deposits in the Naracoorte Caves, South Australia. *Journal of Quaternary Science*, 16(1), 49-59.
- HOCKNULL, S. A., ZHAO, J. X., FENG, Y. X., & WEBB, G. E. (2007). Responses of Quaternary rainforest vertebrates to climate change in Australia. *Earth and Planetary Science Letters*, 264(1-2), 317-331. doi: <https://doi.org/10.1016/j.epsl.2007.10.004>.
- HUNT, C. O., & FIACCONI, M. (2018). Pollen taphonomy of cave sediments: What does the pollen record in caves tell us about external environments and how do we assess its reliability? *Quaternary International*, 485, 68-75. doi: <https://doi.org/10.1016/j.quaint.2017.05.016>.

- JENNINGS, J. N. (1968). Syngenetic karst in Australia. In P. W. Williams & J. N. Jennings (Eds.), *Contributions to the Study of Karst, Research School of Pacific Studies, Australian National University*. (pp. 41-110). Department of Geography Publication.
- JENSEN, M. P., ARYAL, B. P., GORMAN-LEWIS, D., PAUNESKU, T., LAI, B., VOGT, S., & WOLOSCHAK, G. E. (2012). Submicron hard X-ray fluorescence imaging of synthetic elements. *Analytica Chimica Acta*, 722, 21-28. doi: 10.1016/j.aca.2012.01.064.
- JOUZEL, J., STIÉVENARD, M., JOHNSEN, S. J., LANDAIS, A., MASSON-DELMOTTE, V., SVEINBJORNSDOTTIR, A., ... WHITE, J. W. C. (2007). The GRIP deuterium-excess record. *Quaternary Science Reviews*, 26(1-2), 1-17. doi: <https://doi.org/10.1016/j.quascirev.2006.07.015>.
- KEMP, C. W., TIBBY, J., ARNOLD, L. J., BARR, C., GADD, P. S., MARSHALL, J. C., ... JACOBSEN, G. E. (2020). Climates of the last three interglacials in subtropical eastern Australia inferred from wetland sediment geochemistry. *Palaeogeography, Palaeoclimatology, Palaeoecology*, 538, 109463.
- KERSHAW, A. P., MCKENZIE, G. M., PORCH, N., ROBERTS, R. G., BROWN, J., HEIJNIS, H., ... NEWALL, P. R. (2007). A high-resolution record of vegetation and climate through the last glacial cycle from Caledonia Fen, southeastern highlands of Australia. *Journal of Quaternary Science*, 22(5), 481-500. doi: 10.1002/jqs.1127.
- KOHLI, R. (2019). Methods for assessing surface cleanliness. In R. Kohli & K. L. Mittal (Eds.), *Developments in surface contamination and cleaning, volume 12* (pp. 23-105). Cambridge, MA: Elsevier Inc.
- LEWIS, I. D. (2019). South Australian geology and the State Heritage Register: an example of geoconservation of the Naracoorte Caves complex and karst environment. *Australian Journal of Earth Sciences*, 66(6), 785-792.
- LEWIS, R. J., TIBBY, J., ARNOLD, L. J., GADD, P., JACOBSEN, G., BARR, ... MOSS, E. Patterns of aeolian deposition in subtropical Australia through the last glacial and deglacial phases. *Quaternary Research*, submitted.
- LI, Q., MCGOWRAN, B., & WHITE, M. R. (2000). Sequences and biofacies packages in the mid-Cenozoic Gambier Limestone, South Australia: reappraisal of foraminiferal evidence. *Australian Journal of Earth Sciences*, 47, 955-970.
- LIPAR, M., WEBB, J. A., WHITE, S. Q., & GRIMES, K. G. (2015). The genesis of solution pipes: Evidence from the Middle-Late Pleistocene Bridgewater Formation calcarenite, southeastern Australia. *Geomorphology*, 246, 90-103. doi: <http://dx.doi.org/10.1016/j.geomorph.2015.06.013>.
- LIPAR, M., WEBB, J. A., CUPPER, M. L., & WANG, N. (2017). Aeolianite, calcrete/microbialite and karst in southwestern Australia as indicators of Middle to Late Quaternary palaeoclimates. *Palaeogeography, Palaeoclimatology, Palaeoecology*, 470, 11-29. doi: <http://dx.doi.org/10.1016/j.palaeo.2016.12.019>.
- LISIECKI, L. E., & RAYMO, M. E. (2005). Pliocene-Pleistocene stack of globally distributed benthic stable oxygen isotope records. Retrieved from: <https://doi.org/10.1594/PANGAEA.704257>.
- MACKEN, A. C., JANKOWSKI, N. R., PRICE, G. J., BESTLAND, E. A., REED, E. H., PRIDEAUX, G. J., & ROBERTS, R. G. (2011). Application of sedimentary and chronological analyses to refine the depositional context of a Late Pleistocene vertebrate deposit, Naracoorte, South Australia. *Quaternary Science Reviews*, 30(19), 2690-2702. doi: <https://doi.org/10.1016/j.quascirev.2011.05.023>.
- MACKEN, A. C., MCDOWELL, M. C., BARTHOLOMEUSZ, D. N., & REED, E. H. (2013a). Chronology and stratigraphy of the Wet Cave vertebrate fossil deposit, Naracoorte, and relationship to paleoclimatic conditions of the Last Glacial Cycle in south-eastern Australia. *Australian Journal of Earth Sciences*, 60, 271-281. Retrieved from: <http://dx.doi.org/10.1080/08120099.2013.758657>.
- MACKEN, A. C., STAFF, R. A., & REED, E. H. (2013b). Bayesian age-depth modelling of Late Quaternary deposits from Wet and Blanche Caves, Naracoorte, South Australia: A framework for comparative faunal analyses. *Quaternary Geochronology*, 17, 26-43. Retrieved from: <http://dx.doi.org/10.1016/j.quageo.2013.03.001>.
- MORIARTY, K. C., MCCULLOCH, M. T., WELLS, R. T., & MCDOWELL, M. C. (2000). Mid-Pleistocene cave fills, megafaunal remains and climate change at Naracoorte, South Australia: towards a predictive model using U-Th dating of speleothems. *Palaeogeography, Palaeoclimatology, Palaeoecology*, 159(1), 113-143. doi: [https://doi.org/10.1016/S0031-0182\(00\)00036-5](https://doi.org/10.1016/S0031-0182(00)00036-5).
- MOSS, P. T., & KERSHAW, A. P. (2007). A late Quaternary marine palynological record (oxygen isotope stages 1 to 7) for the humid tropics of northeastern Australia based on ODP Site 820. *Palaeogeography, Palaeoclimatology, Palaeoecology*, 251, 4-22.

- MURRAY, A. S., & WINTLE, A. G. (2000). Luminescence dating of quartz using an improved single-aliquot regenerative-dose protocol. *Radiation Measurements*, 32(1), 57-73. doi: [https://doi.org/10.1016/S1350-4487\(99\)00253-X](https://doi.org/10.1016/S1350-4487(99)00253-X).
- NATHAN, R. P., THOMAS, P. J., JAIN, M., MURRAY, A. S., & RHODES, E. J. (2003). Environmental dose rate heterogeneity of beta radiation and its implications for luminescence dating: Monte Carlo modelling and experimental validation. *Radiation Measurements*, 37(4-5), 305-313. Retrieved from: [https://doi.org/10.1016/S1350-4487\(03\)00008-8](https://doi.org/10.1016/S1350-4487(03)00008-8).
- PATE, F. D., MCDOWELL, M. C., WELLS, R. T., & SMITH, A. M. (2002). Last recorded evidence for megafauna at Wet Cave, Naracoorte, South Australia 45,000 years ago. *Australian Archaeology*, 54, 53-55.
- PATE, F. D., MCDOWELL, M. C., WELLS, R. T., & SMITH, A. M. (2006). Additional AMS radiocarbon dates for Wet Cave and the timing of megafaunal extinctions in the Naracoorte region of South Australia. *Alcheringa: An Australasian Journal of Palaeontology*, 30, 277-279. doi: 10.1080/03115510609506866.
- PRESCOTT, J. R., & HUTTON, J. T. (1994). Cosmic ray contributions to dose rates for luminescence and ESR dating: Large depths and long-term time variations. *Radiation Measurements*, 23(2), 497-500. doi: [https://doi.org/10.1016/1350-4487\(94\)90086-8](https://doi.org/10.1016/1350-4487(94)90086-8).
- PRIDEAUX, G. J., ROBERTS, R. G., MEGIRIAN, D., WESTAWAY, K. E., HELLSTROM, J. C., & OLLEY, J. M. (2007). Mammalian responses to Pleistocene climate change in southeastern Australia. *Geology*, 35(1), 33-36. doi: 10.1130/G23070A.1.
- PRIYA. (2018). *Reconstructing the late Pleistocene climate sequence at Alexandra Cave, Naracoorte, South Australia, using single-grain Optically Stimulated Luminescence dating and palaeoenvironmental proxies*. (Honours thesis, The University of Adelaide, South Australia).
- REED, E. H. (2008). Pinning down the pitfall: entry points for Pleistocene vertebrate remains and sediments in the Fossil Chamber, Victoria Fossil Cave, Naracoorte, South Australia. *Quaternary Australasia*, 25(2), 2-8.
- ROBERTS, R. G., FLANNERY, T. F., AYLIFFE, L. K., YOSHIDA, H., OLLEY, J. M., PRIDEAUX, G. J., ... SMITH, B. L. (2001). New ages for the last Australian megafauna continent-wide extinction about 46,000 years ago. *Science*, 292(5523), 1888-1892. doi: 10.1126/science.1060264.
- ST PIERRE, E., ZHAO, J., FENG, Y., & REED, E. (2012). U-series dating of soda straw stalactites from excavated deposits: method development and application to Blanche Cave, Naracoorte, South Australia. *Journal of Archaeological Science*, 39(4), 922-930. doi: <https://doi.org/10.1016/j.jas.2011.10.027>.
- STIRLING, C. H., ESAT, T. M., LAMBECK, K., MCCULLOCH, M. T., BLAKE, S. G., LEE, D. C., & HALLIDAY, A. N. (2001). Orbital Forcing of the Marine Isotope Stage 9 Interglacial. *Science*, 291, 290-293.
- TORAYA, H. (2016). A new method for quantitative phase analysis using X-ray powder diffraction: direct derivation of weight fractions from observed integrated intensities and chemical compositions of individual phases. *Journal of Applied Crystallography*, 49, 1508-1516.
- VERMEESCH, P. (2012). On the visualisation of detrital age distributions. *Chemical Geology*, 312-313, 190-194. doi: <https://doi.org/10.1016/j.chemgeo.2012.04.021>.
- WELLS, R. T., MORIARTY, K., & WILLIAMS, D. L. G. (1984). The fossil vertebrate deposits of Victoria Fossil Cave Naracoorte: an introduction to the geology and fauna. *The Australian Zoologist*, 21(4), 305-333.
- WHITE, S., & WEBB, J. A. (2015). The influence of tectonics on flank margin cave formation on a passive continental margin: Naracoorte, Southeastern Australia. *Geomorphology*, 229, 58-72. doi: <https://doi.org/10.1016/j.geomorph.2014.09.003>.

## APPENDIX A: FIELD SAMPLING METHODS

Two replicate 1 m-long sediment cores ( $\phi = 5$  cm) were taken from the southeast side of Cone 1 (Figure 3), approximately 30 cm apart (Core 1 & Core 2). Each PVC core was hammered into the cone deposit perpendicular to the surface profile in order to traverse as much of the original accumulation profile as possible and to ensure the bedding planes were not crosscut at an oblique angle (Figure 4a). Upon extraction, the ends of the cores were packed tightly with non-absorbent materials and sealed with opaque bags and duct tape to prevent any light contamination during transportation. The holes left behind by the core extractions were plugged and labelled to minimise site impacts.

On the opposite side of Cone 1 (at Pit 1), a face was cleared (~40 cm high, ~30 cm wide), and a standard OSL dating sample was taken (SMT20-A) by placing a 20 cm opaque metal cylinder into the sediment face (Figure 4b). Field gamma-ray spectrometry measurements were performed in the OSL sample position to calculate the gamma dose rate using a portable Canberra Instruments NaI:Tl detector connected to an InSpector 1000 digital multichannel analyser (Arnold et al., 2012). Additional bulk sediment (~500 g) was collected from the OSL sample position for laboratory beta dose rate and water attenuation evaluations. Geochemistry and pollen sediment samples (~100 g) were collected from the cleaned vertical face of Pit 1 at 5 cm intervals (S1–S6) using a leaf trowel.

The sediment floor was sampled towards the middle of the main chamber by exposing a second pit location (Pit 2) (Figure 3). A small (~33 cm high, ~40 cm wide) vertical exposure face was cleared, and a second OSL sample was taken using a 20 cm metal tube (SMT20-B) (Figure 4c). *In situ* dosimetry measurements were performed and bulk sediment samples were obtained, as described above. Geochemistry and pollen samples were additionally collected at 5 cm intervals (S7–S11) from the vertical exposure.

A ~105 cm high, ~40 cm wide vertical exposure was made in the side of Cone 2 (Pit 3) (Figure 3), and three small metal tube OSL samples were taken (SMT20-C, SMT20-D, & SMT20-E) from the top, middle, and bottom layers of the exposed stratigraphy (Figure 4d). After undertaking gamma spectrometry readings and collecting extra materials for beta dose rate and water content analyses, geochemistry samples were collected at intervals of 10 cm (lower resolution given the larger size of the exposure) (S12–S22).

Finally, a “modern analogue” OSL dating sample (SMT20-MA) was taken from sediments that are actively accumulating at the base of the current solution pipe (Figure 3) to verify whether the bleaching assumption of OSL dating is upheld in this depositional setting. This sample was collected 3.5 m from the solution pipe opening beyond the zone affected by natural daylight. The upper 3 cm of undistributed surface sediment was collected in an opaque bag and sealed, before performing *in situ* gamma spectrometry measurements and collecting bulk dosimetry material.



## APPENDIX B: QUALITY ASSURANCE CRITERIA

Rejection criteria for SMT samples.

Sample Name	SMT20-A	SMT20-B	SMT20-C	SMT20-D	SMT20-E	SMT20-MA
<b>Total Measured Grains</b>	600	600	600	600	600	600
<b>Reasons for rejecting grains from D<sub>e</sub> analysis</b>						
<i>SAR rejection criteria:</i>	%	%	%	%	%	%
NAT <3sigma BG	7	7	6	8	9	5
Poor Low R ratio	26	24	29	26	31	23
Poor High R ratio	11	9	10	10	11	12
Depletion by IR	3	3	3	3	3	2
Recuperation >5%	1	1	1	1	2	5
<i>Other criteria:</i>						
Non-intercepting grains	12	6	14	11	7	8
Poor DRC / anomalous behaviour	12	16	19	18	20	10
<b>Sum of rejected grains (%)</b>	71	66	83	78	82	66
<b>Sum of accepted grains (%)</b>	29	34	17	22	18	34

Continued...

<b>Sample Name</b>	<b>SMT20-C19</b>	<b>SMT20-C36</b>	<b>SMT20-C55</b>	<b>SMT20-C65</b>	<b>SMT20-C94</b>
<b>Total Measured Grains</b>	600	600	600	600	600
<b>Reasons for rejecting grains from D<sub>e</sub> analysis</b>					
<i>SAR rejection criteria:</i>	%	%	%	%	%
NAT <3sigma BG	9	3	6	10	7
Poor Low R ratio	22	26	23	31	28
Poor High R ratio	11	9	9	12	12
Depletion by IR	4	3	3	3	3
Recuperation >5%	1	2	2	2	2
<i>Other criteria:</i>					
Non-intercepting grains	10	12	18	9	6
Poor DRC / anomalous behaviour	21	17	15	18	18
<b>Sum of rejected grains (%)</b>	<b>76</b>	<b>71</b>	<b>74</b>	<b>85</b>	<b>75</b>
<b>Sum of accepted grains (%)</b>	<b>24</b>	<b>29</b>	<b>26</b>	<b>15</b>	<b>25</b>

## APPENDIX C: METHODS FOR EXTERNAL GEOCHEMICAL ANALYSES

### XRF METHODS

The complete major and trace elemental composition of each sample was determined using a Spectro Ametek XEPOS III energy dispersive XRF spectrometer at the University of Wollongong. The trace elemental data was measured using pressed powder pellets (~5 g of powdered sample combined with ~10 drops of PVA solution, pressed into an Al cup at 2500 psi). The pressed pellet was dried at 70 °C for >2 hours and once dry, was weighed to 2 decimal places. The major elemental data was obtained from the analysis of glass-fusion beads using one of three fluxes (pure Lithium Metaborate (LiBO<sub>4</sub>) or mixtures of Lithium Metaborate and Lithium Tetraborate (Li<sub>2</sub>B<sub>4</sub>O<sub>7</sub>); which were selected according to an assessment of the concentration of Si, Ca and Fe in each sample estimated from an analysis of the pressed pellet. The glass beads were made using ~0.4 g of powdered sample material and ~4 g of flux). Samples with >1000ppm S or >300 Cu were oxidised using 5 mL of Lithium Nitrate prior to preparation of the glass fusion bead to prevent damage of the platinum crucibles used to prepare the glass beads. Two geological reference materials were run as unknowns alongside the samples to ensure the results were accurate. The major elemental data was produced using the volatile content obtained from a loss-on-ignition (LOI) measurement of each sample (see below). The results are recorded on a volatile-free basis. The iron concentration for each sample is reported as total Fe<sub>2</sub>O<sub>3</sub>.

Loss on ignition (LOI): Empty crucibles were heated at 1100 °C for >2 hours. The crucibles were removed from the furnace and weighed after they had been placed on a granite slab and cooled sufficiently enough to be handled (15–20 minutes). ~1 g of sample material was inserted into each crucible and weighed. The crucibles were returned to the furnace for two hours at 1100 °C and weighed after heating, and the differences in weight were used to calculate the LOI.

### XRD METHODS

The SMT samples (processed prior using a Retch MM400 ball mill) were further ground (dry) by hand using an agate pestle and mortar. A small aliquot of each sample was packed into an individual aluminium sample cup and flattened using a glass microscope slide with a roughened surface to minimise the preferred orientation due to packing the crystallites.

The diffraction profile of each sample was measured using a ThermoFisher ARL Equinox 1000 X-ray diffractometer (XRD) equipped with a Panalytical short fine focus copper X-ray tube and a germanium monochromator. The instrument also uses a detector gas (85% argon-15% ethane detector gas at 99.9% purity. The peak positions are calibrated using Y<sub>2</sub>O<sub>3</sub>, with calibrations being conducted on a monthly basis. The instrument uses a curved detector and an asymmetric flat plate geometry, which means that the diffraction spectra are recorded from low to high 2-theta synchronously. This means that the signal-to-noise ratio is improved with longer counting times. The samples were measured using an incidence angle of 4 degrees, resulting in diffraction peaks being measured between 4 degrees and 115 degrees 2-theta. Each sample

examined during this study was measured for 60 minutes. Each sample was rotated at a rate of 9 revolutions/minute during the analysis.

The mineral phase identification was conducted using the software Match! (version 3.10.2.173) together with the Crystallographic Open Database (Inorganic, REV248644, 3 March 2020). The quantity of the various phases was estimated using the Direct Derivation method (Toraya 2016). Minor amounts of aluminium were detected above background levels in several samples. Where present, this was taken to reflect small components of the aluminium sample cup.

## **APPENDIX D: POLLEN LABORATORY PROCESS**

### **Stage 1: Sub-Sampling**

Subsample 4 cm<sup>3</sup> of sediment samples (x4) and sieve at 250 µm to collect <250 µm fraction. Label tubes twice and assign numbers.

### **Stage 2: Potassium Hydroxide (KOH – 10%)**

Pour 5 mL of 10% KOH into each tube and mix using a vibrating mixer. Leaving the tubes slightly open, place them into a hot water bath (80–100 °C) for 30 minutes. Seal and mix again, returning to the water bath for another ~15 minutes. Mix again.

Pour the entire contents of each sample into a 50 mL tube through a 100 µm sieve, using DI water to rinse all the sediment through the sieve until the tube is full (make sure to wash the sieve after each sample in an ultrasonic bath to ensure no contamination). Centrifuge at 3000 rpm for 3 minutes. Decant the supernatant into the appropriate waste container in the fume hood and transfer the samples back into 25mL tubes. Rinse with DI water, mix, and centrifuge again at 3000 rpm for 3 minutes. Decant supernatant. Repeat the rinsing step until supernatant is clear (at least twice).

### **Stage 3: Hydrochloric Acid (HCl – 10%)**

Add 1 Lycopodium tablet into each sample tube and add 2 mL of 10% HCl. Wait for lycopodium tablet to dissolve with the lid resting on top. Fill each tube up to 7 mL with 10% HCl and mix. Place the tubes in a hot water bath (80–100 °C) for ~10 minutes with lid slightly on. Fill tubes to top with DI water, and centrifuge at 3000 rpm for 3 minutes. Decant the supernatant into appropriate waste container. Rinse with DI water, mix, and centrifuge again at 3000 rpm for 3 minutes. Decant the supernatant and repeat rinsing until supernatant is clear.

### **Stage 4: Heavy Liquid Separation – LST**

Add 5 mL of LST to each sample using a pipette and mix. Centrifuge at 2500 rpm for 30 minutes. Ensure that samples have separated and there is no floating debris in the solution. Immerse the bottom 2 mL of each tube in dry ice until frozen. Decant the top (pollen concentrate) into clean 50 mL tubes and fill to the top with DI water (decant the frozen sediment layer into heavy liquid waste container). Transfer pollen slowly into 15 mL tubes and centrifuge at 3000 rpm for 3 minutes. Wash 50 mL tubes.

### **Stage 5: Acetolysis (Glacial Acetic Acid & Acetic Anhydride)**

Fill each tube with 5 mL glacial acetic acid, mix, and centrifuge at 3000 rpm for 3 minutes. Decant supernatant into waste container. Fill each tube with 4.5 mL acetic anhydride using dispenser and mix. Then, fill each tube with 0.5 mL of sulphuric acid. Mix thoroughly with a plastic stirring rod (reaction will be exothermic and cause the tubes to heat up). Place the tubes into a hot water bath (80–100 °C) for 3 minutes with lids slightly open. Seal lids and mix again. Centrifuge at 3000 rpm for 3 minutes with lids slightly open and decant the supernatant. Fill each tube with 5 mL of glacial acetic acid using dispenser and mix. Centrifuge at 3000 rpm for 3 minutes, then decant the supernatant. Rinse with DI water, mix, and centrifuge again at 3000 rpm for 3 minutes, decanting the supernatant. Repeat rinsing until supernatant is clear.

**Stage 6: Ethanol**

Start by labelling x4 15 mL tubes and transfer the samples into these using ethanol. Seal the sample tube and place it inside the 25 mL tube so that it rests at the top. Centrifuge at 3000 rpm for 3 minutes and decant the supernatant. Add 0.5–1 mL (a few drops) of glycerine to each 5 mL sample tube and stir thoroughly with a toothpick. Leave the toothpick in each sample and cover overnight.

**Stage 7: Mounting Slides**

Label slides twice and mix sample again. Add 2–3 drops onto each slide and manipulate into an “X”. Drop the coverslip onto the slide and manipulate with toothpick if necessary. Sample solution should spread out. Paint nail polish into the edges of the coverslip to seal. Wait ~10 minutes for them to dry before viewing through microscope.

**APPENDIX E: XRF GEOCHEMISTRY RESULTS**

Appendix E, Table 1: Major Elements

Sample	Na <sub>2</sub> O	Na	MgO	Mg	Al <sub>2</sub> O <sub>3</sub>	Al	SiO <sub>2</sub>	Si	P <sub>2</sub> O <sub>5</sub>	P	K <sub>2</sub> O	K	CaO	Ca	TiO <sub>2</sub>	Ti	MnO	Mn	Fe <sub>2</sub> O <sub>3</sub>	Fe	LOI	Total
	%	%	%	%	%	%	%	%	%	%	%	%	%	%	%	%	%	%	%	%	%	%
		0.7419		0.603		0.5293		0.4674		0.4364		0.8301		0.7147		0.5994		0.7745		0.699		
<b>XRF for Cave Sediments</b>																						
SMT20_S1	< 0.020	0.015	1.21	0.73	13.05	6.91	67.36	31.48	0.09	0.04	0.70	0.58	2.05	1.47	0.57	0.34	0.01	0.01	5.67	3.97	9.15	99.86
SMT20_S2	0.13	0.10	1.55	0.93	17.86	9.45	58.72	27.45	0.03	0.01	0.76	0.63	1.68	1.20	0.70	0.42	0.01	0.01	7.61	5.32	10.81	99.86
SMT20_S3	< 0.020	0.015	1.01	0.61	13.44	7.11	67.02	31.33	0.03	0.01	0.62	0.52	2.13	1.52	0.53	0.32	0.01	0.01	5.93	4.15	9.14	99.87
SMT20_S4	< 0.020	0.015	0.63	0.38	5.00	2.65	57.83	27.03	0.03	0.01	0.26	0.21	16.34	11.68	0.22	0.13	0.01	0.01	2.30	1.61	17.23	99.85
SMT20_S5	< 0.020	0.015	0.24	0.14	3.45	1.82	78.70	36.78	0.01	0.00	0.22	0.18	7.42	5.30	0.19	0.11	0.01	0.01	1.50	1.05	8.19	99.91
SMT20_S6	< 0.020	0.015	0.15	0.09	1.75	0.92	81.06	37.89	0.00	0.00	0.14	0.11	8.18	5.85	0.14	0.08	0.01	0.00	0.78	0.55	7.69	99.88
SMT20_S7	< 0.020	0.015	< 0.0083	0.0050	0.97	0.51	93.41	43.66	0.13	0.06	0.11	0.09	2.28	1.63	0.10	0.06	0.01	0.00	0.47	0.33	2.32	99.79
SMT20_S8	< 0.020	0.015	< 0.0083	0.0050	1.61	0.85	94.91	44.36	0.03	0.01	0.08	0.07	1.19	0.85	0.08	0.05	0.00	0.00	0.29	0.20	1.74	99.93
SMT20_S9	< 0.020	0.015	< 0.0083	0.0050	0.98	0.52	96.83	45.26	0.09	0.04	0.11	0.09	0.52	0.37	0.11	0.07	0.00	0.00	0.37	0.26	0.91	99.91
SMT20_S10	< 0.020	0.015	< 0.0083	0.0050	0.58	0.31	98.02	45.81	< 0.0012	0.0005	0.06	0.05	0.41	0.29	0.06	0.04	0.00	0.00	0.24	0.17	0.61	99.98
SMT20_S11	< 0.020	0.015	< 0.0083	0.0050	1.14	0.60	97.30	45.48	0.01	0.00	0.07	0.06	0.27	0.19	0.07	0.04	0.00	0.00	0.26	0.18	0.79	99.92
SMT20_S12	< 0.020	0.015	0.04	0.02	3.50	1.85	89.85	42.00	< 0.0012	0.0005	0.18	0.15	1.55	1.11	0.16	0.09	0.01	0.00	1.38	0.96	3.29	99.95
SMT20_S13	< 0.020	0.015	0.01	0.01	2.79	1.48	62.29	29.11	0.15	0.06	0.13	0.11	0.14	0.10	0.12	0.07	0.00	0.00	1.06	0.74	33.26	99.95
SMT20_S14	< 0.020	0.015	< 0.0083	0.0050	2.77	1.47	93.50	43.70	< 0.0012	0.0005	0.17	0.14	0.15	0.11	0.17	0.10	0.01	0.01	1.17	0.82	2.03	99.97
SMT20_S15	< 0.020	0.015	< 0.0083	0.0050	2.56	1.35	94.01	43.94	< 0.0012	0.0005	0.16	0.13	0.13	0.09	0.18	0.11	0.00	0.00	1.13	0.79	1.76	99.91
SMT20_S16	< 0.020	0.015	< 0.0083	0.0050	2.21	1.17	94.74	44.28	< 0.0012	0.0005	0.14	0.11	0.11	0.08	0.15	0.09	0.00	0.00	0.94	0.66	1.62	99.90
SMT20_S17	< 0.020	0.015	< 0.0083	0.0050	3.20	1.69	92.51	43.24	< 0.0012	0.0005	0.17	0.14	0.15	0.11	0.18	0.11	0.00	0.00	1.31	0.91	2.37	99.89
SMT20_S18	< 0.020	0.015	< 0.0083	0.0050	3.27	1.73	92.85	43.40	< 0.0012	0.0005	0.19	0.16	0.14	0.10	0.14	0.09	0.00	0.00	1.33	0.93	2.04	99.96
SMT20_S19	< 0.020	0.015	< 0.0083	0.0050	2.66	1.41	94.28	44.07	< 0.0012	0.0005	0.14	0.12	0.12	0.08	0.15	0.09	0.00	0.00	0.94	0.66	1.63	99.92
SMT20_S20	< 0.020	0.015	< 0.0083	0.0050	2.11	1.12	94.87	44.34	< 0.0012	0.0005	0.14	0.11	0.10	0.07	0.14	0.09	0.00	0.00	0.90	0.63	1.66	99.92
SMT20_S21	< 0.020	0.015	< 0.0083	0.0050	2.06	1.09	95.15	44.47	< 0.0012	0.0005	0.16	0.14	0.10	0.07	0.15	0.09	0.00	0.00	0.89	0.62	1.40	99.92
SMT20_S22	< 0.020	0.015	< 0.0083	0.0050	1.65	0.88	96.06	44.90	< 0.0012	0.0005	0.15	0.13	0.09	0.06	0.14	0.08	0.00	0.00	0.69	0.48	1.11	99.89

Rhianna Power  
Cone Deposit Formation Dynamics

Sample	Na <sub>2</sub> O	Na	MgO	Mg	Al <sub>2</sub> O <sub>3</sub>	Al	SiO <sub>2</sub>	Si	P <sub>2</sub> O <sub>5</sub>	P	K <sub>2</sub> O	K	CaO	Ca	TiO <sub>2</sub>	Ti	MnO	Mn	Fe <sub>2</sub> O <sub>3</sub>	Fe	LOI	Total
<b>XRF for Core Sequence 2</b>																						
SMT20_I1	< 0.020	0.015	0.32	0.19	5.42	2.87	87.25	40.78	0.01	0.01	0.30	0.25	0.34	0.24	0.25	0.15	0.01	0.00	2.17	1.51	3.82	99.87
SMT20_I2	< 0.020	0.015	0.08	0.05	3.44	1.82	91.70	42.86	< 0.0012	0.0005	0.22	0.18	0.20	0.15	0.19	0.12	0.01	0.00	1.45	1.01	2.63	99.93
SMT20_I3	< 0.020	0.015	0.14	0.09	4.07	2.15	90.63	42.36	< 0.0012	0.0005	0.24	0.20	0.12	0.09	0.17	0.10	0.01	0.01	1.66	1.16	2.88	99.91
SMT20_I4	< 0.020	0.015	< 0.0083	0.0050	1.86	0.99	95.54	44.66	< 0.0012	0.0005	0.15	0.13	0.06	0.04	0.15	0.09	0.00	0.00	0.89	0.62	1.26	99.93
SMT20_I5	< 0.020	0.015	< 0.0083	0.0050	3.10	1.64	93.75	43.82	0.04	0.02	0.21	0.17	0.08	0.06	0.17	0.10	0.00	0.00	0.95	0.66	1.55	99.85
SMT20_I6	< 0.020	0.015	0.06	0.03	2.87	1.52	92.77	43.36	< 0.0012	0.0005	0.21	0.18	0.21	0.15	0.16	0.10	0.01	0.00	1.28	0.90	2.37	99.94
SMT20_I7	< 0.020	0.015	0.09	0.05	2.98	1.58	92.52	43.24	< 0.0012	0.0005	0.22	0.18	0.15	0.11	0.17	0.10	0.00	0.00	1.36	0.95	2.45	99.94
SMT20_I8	< 0.020	0.015	0.30	0.18	4.36	2.31	88.51	41.37	< 0.0012	0.0005	0.32	0.27	0.49	0.35	0.22	0.13	0.01	0.01	1.99	1.39	3.74	99.93
SMT20_I9	< 0.020	0.015	0.19	0.11	3.64	1.93	90.22	42.17	< 0.0014	0.0006	0.28	0.23	0.70	0.50	0.18	0.11	0.01	0.01	1.57	1.10	3.15	99.94
SMT20_I10	< 0.020	0.015	0.50	0.30	2.66	1.41	62.10	29.03	0.36	0.16	0.20	0.17	16.92	12.09	0.14	0.08	0.01	0.01	1.22	0.85	15.73	99.84
SMT20_I11	0.74	0.55	0.93	0.56	1.53	0.81	24.94	11.66	1.01	0.44	0.09	0.08	37.54	26.83	0.07	0.04	0.01	0.01	0.73	0.51	32.16	99.77
SMT20_I12	0.13	0.10	0.69	0.42	2.29	1.21	47.72	22.30	0.27	0.12	0.16	0.13	25.19	18.00	0.11	0.07	0.01	0.01	1.06	0.74	22.20	99.84
SMT20_I13	0.04	0.03	0.62	0.37	2.50	1.32	55.42	25.90	0.04	0.02	0.19	0.16	20.88	14.92	0.13	0.08	0.01	0.01	1.15	0.80	18.93	99.90
SMT20_I14	< 0.020	0.015	0.41	0.24	2.84	1.50	67.42	31.51	0.03	0.01	0.21	0.17	14.23	10.17	0.14	0.08	0.01	0.01	1.10	0.77	13.50	99.88
SMT20_I15	< 0.020	0.015	0.37	0.22	2.06	1.09	65.55	30.64	0.08	0.03	0.16	0.14	16.01	11.44	0.13	0.08	0.01	0.01	0.96	0.67	14.56	99.89
SMT20_I16	< 0.020	0.015	0.31	0.19	2.15	1.14	68.94	32.22	0.04	0.02	0.17	0.14	14.21	10.16	0.12	0.07	0.01	0.01	0.96	0.67	12.99	99.90
SMT20_I17	< 0.020	0.015	0.33	0.20	1.86	0.99	68.20	31.88	0.08	0.04	0.15	0.12	14.92	10.66	0.12	0.07	0.01	0.01	0.84	0.59	13.38	99.89
<b>XRF for Modern Analogue</b>																						
SMT20_MA	< 0.020		0.00		4.83		79.11		0.07		0.25		2.79		0.22		0.01		2.24		10.33	99.86
<b>AVERAGES</b>																						
Pit 1	0.13		0.80		9.09		68.45		0.03		0.45		6.30		0.39		0.01		3.97		10.37	
Pit 2					1.06		96.09		0.06		0.09		0.93		0.08		0.00		0.33		1.27	
Pit 3			0.02		2.62		90.92		0.15		0.16		0.25		0.15		0.00		1.07		4.74	
Core 2	0.30		0.35		2.92		75.48		0.20		0.20		9.54		0.16		0.01		1.25		9.84	
MA			0.00		4.83		79.11		0.07		0.25		2.79		0.22		0.01		2.24		10.33	



Appendix E, Table 2: Trace Elements

Sample	S	Cl	V	Cr	Co	Ni	Cu	Zn	Ga	Ge	As	Se	Br	Rb	Sr	Y	Zr	Nb	Cd	Sn	Sb	Cs	Ba	La	Hf	Ta	W	Pb	Th	U
	ppm	ppm	ppm	ppm	ppm	ppm	ppm	ppm	ppm	ppm	ppm	ppm	ppm	ppm	ppm	ppm	ppm	ppm	ppm	ppm	ppm	ppm	ppm	ppm	ppm	ppm	ppm	ppm	ppm	ppm
<b>XRF for Cave Sediments</b>																														
SMT20_S1	240.00	166.80	113.90	98.80	19.00	47.90	5.30	24.70	14.10	2.60	18.00	0.20	1.80	59.00	58.80	25.70	148.30	7.50	<2.0	5.00	<3.0	<4.0	88.50	55.00	4.50	4.20	<1.0	15.50	9.00	<1.0
SMT20_S2	113.40	151.80	166.20	109.20	18.90	35.90	4.90	25.70	20.10	2.30	24.20	0.10	0.80	72.60	60.80	31.40	153.20	9.20	<2.0	<3.0	<3.0	<4.0	41.10	50.40	4.60	2.00	<1.0	21.10	13.50	<1.0
SMT20_S3	109.80	72.80	121.60	93.50	16.50	39.20	4.20	19.70	14.90	2.50	20.60	0.10	0.90	56.50	50.60	25.30	135.90	7.20	<2.0	3.60	<3.0	<4.0	50.20	59.30	3.80	2.60	<1.0	14.60	8.70	<0.4
SMT20_S4	441.50	86.50	54.10	54.30	12.50	19.40	3.70	9.20	4.50	1.00	8.80	0.30	3.10	23.60	137.30	20.30	75.40	3.50	<2.0	<3.0	<3.0	<4.0	51.60	45.40	0.30	0.50	<1.0	5.70	3.10	<1.0
SMT20_S5	328.00	71.50	37.80	31.80	10.40	15.50	3.00	6.50	1.90	1.30	5.80	0.10	1.20	17.10	76.70	11.10	105.20	3.10	<2.0	3.60	<3.0	<4.0	44.60	47.30	1.40	2.60	<1.0	3.80	1.50	<1.0
SMT20_S6	347.70	90.90	19.00	26.90	7.10	13.00	2.70	4.00	<0.5	<0.5	3.10	0.10	1.40	9.50	72.10	7.20	77.50	2.00	<2.0	4.90	<3.0	<4.0	13.90	<2.0	0.40	2.40	<1.0	1.60	<1.0	<1.0
SMT20_S7	2268.00	664.30	2.70	103.30	<6.0	36.10	3.80	4.80	<0.5	1.30	1.90	0.20	1.40	5.60	17.30	4.10	55.00	1.10	<2.0	7.40	<3.0	<4.0	32.10	<2.0	0.30	4.30	<1.0	0.70	<1.0	<1.0
SMT20_S8	345.00	272.50	5.50	13.50	<5.3	2.00	2.20	4.30	<0.5	1.40	1.60	0.10	0.90	5.30	11.20	3.40	85.00	1.50	0.70	8.30	<3.0	<4.0	23.00	<2.0	1.10	3.90	<1.0	0.30	<1.0	<1.0
SMT20_S9	482.10	324.80	6.50	23.60	12.00	45.50	2.30	3.60	<0.5	0.70	1.60	0.10	0.80	5.20	9.40	3.40	60.10	1.30	<2.0	5.80	<3.0	<4.0	26.50	37.80	<1.0	11.70	<1.0	0.60	<1.0	<1.0
SMT20_S10	74.30	150.80	3.00	22.10	<5.8	21.60	2.50	2.90	<0.5	1.30	1.10	0.10	0.80	4.10	8.30	3.60	55.50	1.00	<2.0	9.80	<3.0	<4.0	18.80	<2.0	0.30	5.30	<1.0	0.70	<1.0	<1.0
SMT20_S11	60.80	105.10	1.90	15.80	3.10	10.00	1.50	3.00	<0.5	1.10	1.40	0.10	0.70	4.20	6.70	3.30	37.30	1.10	<2.0	7.30	<3.0	<4.0	15.80	<2.0	0.60	5.30	<1.0	0.30	<1.0	<1.0
SMT20_S12	83.40	25.80	28.70	46.80	7.40	7.80	2.90	13.40	2.00	1.50	5.40	<0.1	<0.5	13.00	15.40	8.20	102.30	2.80	<2.0	7.30	<3.0	<4.0	19.00	29.50	1.50	3.70	<1.0	3.20	1.10	<1.0
SMT20_S13	35.10	23.30	43.00	41.80	<13	11.30	5.30	7.70	3.80	1.10	6.70	0.10	<0.5	16.20	10.70	9.80	94.10	2.90	0.50	5.40	<3.0	<4.0	17.90	22.20	0.60	0.70	<1.0	3.90	1.60	<1.0
SMT20_S14	28.00	24.10	31.60	41.30	<8.6	8.20	2.40	5.40	1.20	1.50	4.50	0.10	<0.5	11.10	8.50	7.60	104.00	2.60	<2.0	1.90	<3.0	<4.0	34.40	38.90	2.30	3.70	<1.0	2.80	0.40	<0.3
SMT20_S15	60.50	238.30	21.60	42.80	<8.1	15.60	3.20	5.30	1.30	1.50	4.80	0.10	<0.5	10.20	8.10	7.50	81.70	2.20	<2.0	5.30	<3.0	<4.0	34.50	52.10	0.90	3.80	<1.0	2.80	0.50	<1.0
SMT20_S16	30.60	94.20	18.20	27.00	8.90	6.20	5.60	4.60	1.90	1.10	4.30	<0.1	<0.5	9.30	7.40	7.00	78.20	2.00	<2.0	5.90	<3.0	<4.0	22.10	57.30	<1.0	1.20	<1.0	2.20	<0.3	<1.0
SMT20_S17	25.20	70.80	26.10	23.10	<8.7	7.50	2.40	5.40	1.50	1.60	5.00	0.10	<0.5	11.40	8.60	8.20	64.80	1.80	0.30	2.90	<3.0	<4.0	27.40	<2.0	1.10	4.30	<1.0	2.90	0.60	<1.0
SMT20_S18	32.50	71.50	26.60	48.50	13.40	25.50	6.30	6.10	3.00	1.60	6.10	0.10	<0.5	12.40	8.90	8.50	91.40	2.40	<2.0	7.20	<3.0	<4.0	24.30	56.30	<1.0	2.00	<1.0	2.90	0.70	<1.0
SMT20_S19	32.10	97.50	21.20	48.40	6.70	16.50	2.30	4.50	0.50	1.70	4.30	<0.1	<0.5	9.30	7.40	6.80	70.70	1.90	<2.0	8.10	<3.0	<4.0	27.00	<2.0	1.10	4.90	<1.0	2.10	<1.0	<0.3
SMT20_S20	14.90	70.30	21.30	46.60	5.30	6.20	3.40	4.40	0.80	1.60	4.10	0.10	<0.5	9.10	7.70	6.80	84.70	2.20	<2.0	5.20	<3.0	<4.0	<2.0	<2.0	0.70	3.70	<1.0	2.00	<1.0	<1.0
SMT20_S21	33.70	111.80	20.60	49.10	7.80	4.90	2.90	4.20	<0.2	1.60	3.70	0.10	<0.5	9.00	7.50	6.30	81.70	1.80	<2.0	7.30	<3.0	<4.0	26.30	<2.0	0.70	3.80	<1.0	1.80	<1.0	<1.0
SMT20_S22	32.80	156.10	16.60	56.40	<5.7	12.00	2.80	3.50	<0.5	1.10	3.30	0.10	<0.5	7.80	7.10	5.00	87.60	2.00	0.20	10.30	<3.0	<4.0	22.80	<2.0	1.40	4.50	<1.0	1.50	<1.0	<1.0

Rhianna Power  
Cone Deposit Formation Dynamics

**XRF for Core Sequence 2**

SMT20_I1	1677.00	3173.00	39.60	62.40	18.10	63.50	5.10	8.90	3.80	1.80	9.10	0.10	5.10	23.00	21.10	10.80	108.60	3.80	<2.0	5.60	<3.0	<4.0	20.50	56.40	1.60	6.50	<1.0	5.50	2.60	<1.0
SMT20_I2	600.10	1754.00	33.40	36.30	7.60	7.50	3.80	6.00	2.10	1.60	6.10	0.10	2.20	15.90	14.70	8.10	91.70	3.00	<2.0	6.60	<3.0	<4.0	12.20	<2.0	1.00	3.60	<1.0	3.60	0.90	<1.0
SMT20_I3	733.50	2122.00	39.30	42.70	<12	12.40	3.40	6.70	2.90	1.70	6.80	0.10	2.70	17.80	14.70	8.90	95.10	3.00	<2.0	8.20	<3.0	<4.0	31.90	46.40	1.60	3.40	<1.0	4.50	1.00	<1.0
SMT20_I4	245.80	667.80	17.30	67.60	5.60	5.80	2.20	4.20	<0.5	1.50	3.60	0.10	1.10	9.90	9.20	5.70	74.90	2.10	<2.0	4.70	<3.0	<4.0	35.40	<2.0	1.10	4.40	<1.0	1.90	<1.0	<1.0
SMT20_I5	225.90	728.10	20.10	59.40	8.70	5.30	2.60	5.00	0.60	1.80	4.20	0.10	1.20	11.60	10.10	6.30	101.60	2.40	<2.0	6.50	<3.0	<4.0	30.70	<2.0	1.60	3.70	<1.0	2.20	<0.3	<0.3
SMT20_I6	250.00	889.80	28.50	50.50	9.00	33.80	2.90	6.30	1.50	1.70	5.70	0.10	0.70	16.00	14.00	7.60	98.70	3.00	<2.0	8.40	<3.0	<4.0	36.60	44.90	1.50	5.30	<1.0	3.10	1.30	<1.0
SMT20_I7	173.60	720.40	26.80	49.80	<9.4	24.40	5.90	6.10	2.70	1.70	5.90	0.10	<0.5	14.80	12.10	6.20	76.10	2.20	<2.0	8.50	<3.0	<4.0	22.30	<2.0	<1.0	2.20	<1.0	2.30	0.80	<1.0
SMT20_I8	158.20	680.90	42.20	42.80	13.40	12.10	4.90	9.60	4.40	<0.3	7.10	<0.1	<0.5	24.70	20.10	9.10	97.80	3.10	<2.0	8.00	<3.0	<4.0	21.60	<2.0	1.10	1.40	<1.0	5.00	2.10	<1.0
SMT20_I9	125.40	624.50	32.80	37.70	10.20	8.70	2.80	8.30	2.70	1.80	6.50	0.10	<0.5	20.90	20.70	9.30	102.20	2.70	<2.0	5.90	<3.0	<4.0	32.40	<2.0	2.00	3.30	<1.0	3.00	0.90	<1.0
SMT20_I10	588.10	1020.00	24.00	33.10	10.30	31.70	2.30	7.30	0.40	0.90	4.20	0.20	6.00	15.20	139.50	23.60	59.60	2.20	<2.0	3.10	<3.0	<4.0	26.30	41.10	<1.0	3.60	<1.0	3.00	0.70	<1.0
SMT20_I11	799.60	955.80	10.20	25.50	7.90	19.50	1.40	7.50	<0.5	<0.5	2.50	0.30	12.40	9.60	268.70	9.30	29.10	1.90	<2.0	<3.0	<3.0	<4.0	71.30	9.60	<1.0	<1.0	<1.0	1.00	0.50	0.40
SMT20_I12	645.00	883.10	28.00	21.30	5.80	3.70	2.10	6.60	<0.5	<0.5	3.60	0.20	8.10	13.30	185.20	8.10	44.20	2.00	<2.0	<3.0	<3.0	<4.0	45.50	<2.0	<1.0	<1.0	<1.0	2.50	0.70	<1.0
SMT20_I13	425.30	495.20	22.40	23.80	8.00	4.20	2.20	6.20	0.60	0.80	3.70	0.10	4.50	14.80	133.50	8.00	63.70	2.10	<2.0	<3.0	<3.0	<4.0	43.10	<2.0	<1.0	0.40	<1.0	2.50	<0.4	<0.4
SMT20_I14	432.80	632.50	28.70	31.70	<10	32.50	2.40	6.50	0.50	1.10	3.90	0.10	3.50	14.90	110.20	8.10	67.70	2.30	<2.0	0.90	<3.0	<4.0	37.60	44.40	0.40	3.40	<1.0	2.60	<0.4	<1.0
SMT20_I15	517.50	653.40	25.80	47.30	<18	90.40	4.60	6.50	0.50	1.30	3.30	0.10	4.50	12.20	125.00	7.10	66.40	1.90	<2.0	<3.0	<3.0	<4.0	37.70	19.80	<1.0	6.60	<1.0	2.20	<1.0	<0.4
SMT20_I16	438.90	570.00	20.20	23.10	<6.8	4.30	3.00	5.50	0.60	1.00	3.40	0.20	3.10	12.60	93.20	5.30	49.60	2.10	0.10	2.60	<3.0	<4.0	18.10	44.00	<1.0	0.80	<1.0	2.00	0.90	<0.4
SMT20_I17	487.40	728.40	20.80	23.30	5.60	10.10	1.70	5.20	<0.5	<0.5	2.80	0.10	3.20	10.60	101.20	5.00	46.90	1.60	<2.0	4.00	<3.0	<4.0	31.10	31.90	<1.0	2.40	<1.0	2.00	<1.0	<1.0

**XRF for Modern Age**

SMT20_MA	1149.00	1510.00	48.80	48.90	10.70	20.30	4.60	11.90	3.80	1.40	8.40	0.20	8.50	17.10	43.10	13.20	79.30	3.20	<2.0	11.30	<3.0	<4.0	34.60	49.00	1.30	4.00	<1.0	6.90	2.00	<1.0
----------	---------	---------	-------	-------	-------	-------	------	-------	------	------	------	------	------	-------	-------	-------	-------	------	------	-------	------	------	-------	-------	------	------	------	------	------	------

## APPENDIX F: XRD GEOCHEMISTRY RESULTS

Sample	Quartz	Magnesiochloritoid/Chloritoid	Calcite
<b>XRD for Cave Sediments</b>			
SMT20_S1	69.16%	26.96%	3.86%
SMT20_S2	66.43%	30.93%	2.63%
SMT20_S3	60.00%	33.60%	4.80%
SMT20_S4	32.10%	29.80%	37.10%
SMT20_S5	87.90%		12.10%
SMT20_S6	84.10%		14.60%
SMT20_S7	96.50%		2.70%
SMT20_S8	99.00%		0.50%
SMT20_S9	99.10%		0.90%
SMT20_S10	96.90%		0.10%
SMT20_S11	100.00%		
SMT20_S12	90.30%	7.30%	2.40%
SMT20_S13	99.80%		
SMT20_S14	99.30%		
SMT20_S15	99.10%		
SMT20_S16	99.90%		
SMT20_S17	99.70%		
SMT20_S18	97.60%	2.40%	
SMT20_S19	99.70%		
SMT20_S20	99.40%		
SMT20_S21	98.90%		
SMT20_S22	100.00%		

	Quartz	Magnesiochloritoid/Chloritoid	Calcite	Graphite
<b>XRD for Core Sequence</b>				
SMT20_I1	88.10%	3.30%		7.70%
SMT20_I2	92.70%	5.30%		0.40%
SMT20_I3	94.85%	5.15%		
SMT20_I4	96.30%	2.90%		
SMT20_I5	94.10%	5.60%		
SMT20_I6	97.50%	2.10%		
SMT20_I7	95.10%	4.70%		
SMT20_I8	95.50%	2.90%	0.40%	
SMT20_I9	87.40%	6.40%	2.00%	
SMT20_I10	65.10%	2.20%	32.20%	

<b>SMT20_I11</b>	19.36%	1.66%	79.96%
<b>SMT20_I12</b>	29.60%	7.70%	61.00%
<b>SMT20_I13</b>	56.20%	1.60%	38.40%
<b>SMT20_I14</b>	59.90%	4.50%	34.00%
<b>SMT20_I15</b>	68.76%	8.06%	23.26%
<b>SMT20_I16</b>	58.40%	6.00%	34.10%
<b>SMT20_I17</b>	64.30%	1%	31.50%

**Quartz**

**Magnesiochloritoid/Chloritoid**

**Calcite**

**XRD for Modern Age**

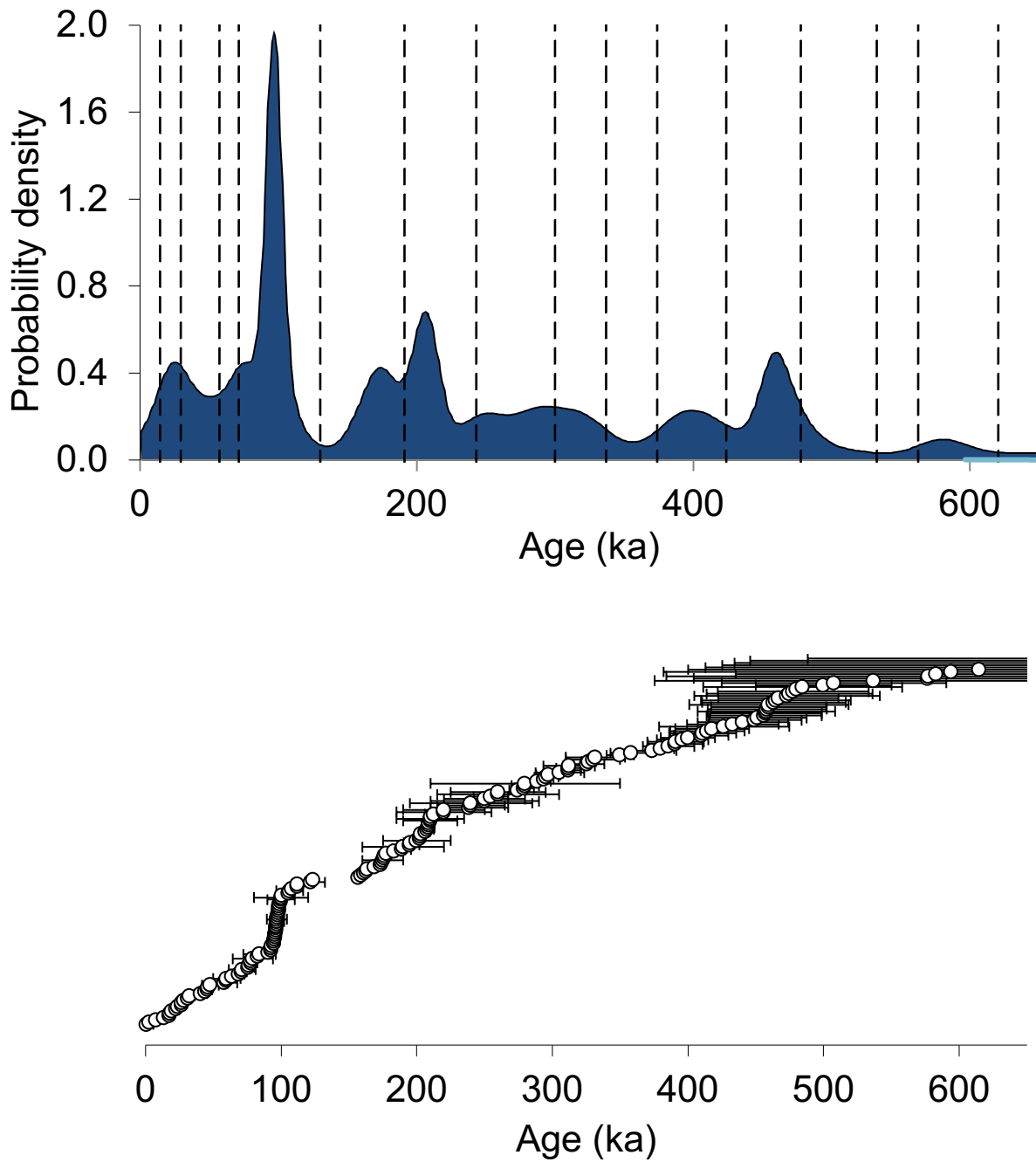
<b>SMT20_MA</b>	92.70%	2.40%	4.20%
-----------------	--------	-------	-------

**APPENDIX G: NCC CONE DEPOSIT DATABASE**

Site	dating technique	age	1 $\sigma$	2 $\sigma$	reference	
Victoria Fossil Cave (Grant Hall)	U-series	46	+1.5/-1	+3/-2	Ayliffe and Veeh 1988	
	U-series	45.9	1.5	3	Ayliffe and Veeh 1988; Moriarty et al 2000	
	U-series	69	2	4	Ayliffe and Veeh 1988	
	U-series	76	+2.5/-2	+5/-4	Ayliffe and Veeh 1988	
	U-series	76.4	0.35	0.7	Moriarty et al 2000	
	OSL	84	8	16	Roberts et al 2001	
	OSL	70	5	10	Macken et al 2011	
	OSL	70	6	12	Macken et al 2011	
	OSL	82	8	16	Macken et al 2011	
	OSL	77	5	10	Macken et al 2011	
	OSL	76	6	12	Macken et al 2011	
	OSL	82	6	12	Macken et al 2011	
	OSL	93	8	16	Macken et al 2011	
	U-series	202.8	1.55	3.1	Moriarty et al 2000	
	U-series	203	1.25	2.5	Moriarty et al 2000	
	U-series	206.7	1.55	3.1	Moriarty et al 2000	
	U-series	207.9	2.4	4.8	Moriarty et al 2000	
	U-series	208.5	2.3	4.6	Moriarty et al 2000	
	U-series	209	2.05	4.1	Moriarty et al 2000	
	U-series	210.6	1	2	Moriarty et al 2000	
	ESR/U-series	128	12	24	Grun et al 2001	
	ESR/U-series	129	13	26	Grun et al 2001	
	ESR/U-series	136	14	28	Grun et al 2001	
	ESR/U-series	121	12	24	Grun et al 2001	
	Victoria Fossil Cave (Fossil Chamber)	U-series	208.9	2.05	4.1	Moriarty et al 2000
		U-series	212.6	3.35	6.7	Moriarty et al 2000
OSL		84	8	16	Roberts et al 2001	
OSL		171	14	28	Roberts et al 2001	
OSL		157	16	32	Roberts et al 2001	
ESR/U-series		283	35	70	Grun et al 2001	
ESR/U-series		282	32	64	Grun et al 2001	
ESR/U-series		373	44	88	Grun et al 2001	
ESR/U-series		437	51	102	Grun et al 2001	
ESR/U-series		441	27	54	Grun et al 2001	
ESR/U-series		544	36	72	Grun et al 2001	
ESR/U-series		443	32	64	Grun et al 2001	
ESR/U-series		445	46	92	Grun et al 2001	
ESR/U-series		463	53	106	Grun et al 2001	
ESR/U-series		425	56	112	Grun et al 2001	
ESR/U-series		360	40	80	Grun et al 2001	
ESR/U-series		439	56	112	Grun et al 2001	

	ESR/U-series	401	64	128	Grun et al 2001
Victoria Fossil Cave (Spring Chamber / Starburst Chamber)	U-series	44.2	0.2	0.4	Moriarty et al 2000; Ayliffe et al 1998
	U-series	40.8	2.3	4.6	Moriarty et al 2000; Ayliffe et al 1998
	U-series	60	5	10	Moriarty et al 2000; Ayliffe and Veeh 1988
	U-series	100	5	10	Moriarty et al 2000; Ayliffe and Veeh 1988
	U-series	100	10	20	Moriarty et al 2000; Ayliffe and Veeh 1988
	U-series	189	3.35	6.7	Moriarty et al 2000; Ayliffe et al 1998
	U-series	173.6	0.65	1.3	Moriarty et al 2000; Ayliffe et al 1998
	U-series	210	10	20	Moriarty et al 2000; Ayliffe et al 1998
	U-series	280	5	10	Moriarty et al 2000; Ayliffe et al 1998
	U-series	326.8	2.7	5.4	Moriarty et al 2000; Ayliffe et al 1998
	U-series	330	10	20	Moriarty et al 2000; Ayliffe et al 1998
	U-series	410	10	20	Moriarty et al 2000; Ayliffe et al 1998
	U-series	350	5	10	Moriarty et al 2000; Ayliffe et al 1998
	U-series	380	5	10	Moriarty et al 2000; Ayliffe et al 1998
	U-series	274.3	3.1	6.2	Moriarty et al 2000; Ayliffe et al 1998
	U-series	300-600			Moriarty et al 2000; Ayliffe et al 1998
	U-series	>500			Moriarty et al 2000; Ayliffe et al 1998
Cathedral Cave (Fossil Chamber)	U-series	95.2	0.65	1.3	Ayliffe et al. 1998; Brown and Wells, 2000; Moriarty et al 2000
	U-series	159.2	1.1	2.2	Ayliffe et al. 1998; Brown and Wells, 2000; Moriarty et al 2000
	ESR	289	19	38	Grun et al 2001
	ESR	292	22	44	Grun et al 2001
	ESR	207	16	32	Grun et al 2001
	ESR	210	14	28	Grun et al 2001
	ESR	206	14	28	Grun et al 2001
	OSL	206	16	32	Prideaux et al 2007
	OSL	231	21	42	Prideaux et al 2007
	OSL	257	21	42	Prideaux et al 2007
	OSL	292	19	38	Prideaux et al 2007
	U-series	279.2	3.6	7.2	Ayliffe et al. 1998; Brown and Wells, 2000; Moriarty et al 2000
	U-series	289	5	10	Prideaux et al 2007
	U-series	297	4.5	9	Prideaux et al 2007
	U-series	396	9.5	19	Prideaux et al 2007
	U-series	400	10	20	Ayliffe et al. 1998; Brown and Wells, 2000; Moriarty et al 2000
	OSL	513	73	146	Prideaux et al 2007
	OSL	535	49	98	Prideaux et al 2007

### APPENDIX H: NCC SPELEOTHEM AGES



Speleothem ages and their probability density (KDE) plot.